Research paper

Vibration control of industrial robot arms by multi-mode time-varying input shaping☆

Dan Kielsholm Thomsen [a,b,*], Rune Søe-Knudsen [b], Ole Balling [a], Xuping Zhang [a]

[a] Aarhus University, Dept. of Engineering., Inge Lehmanns Gade 10, DK-8000 Aarhus C, Denmark
[b] Universal Robots A/S, Energivej 25, DK-5260 Odense S, Denmark

ARTICLE INFO

ABSTRACT

Robot arms exhibit non-ignorable residual vibration during point-to-point motion. Fractional Delay Time-Varying Input Shaping Technology (FD-TVIST) has previously been shown to reduce residual vibrations in robots arms, but requires an accurate estimate of the configuration dependent vibrational behavior. This paper presents a practical set of new tools for identifying and mapping the natural frequencies and damping ratios of dominant vibration modes of a robot arm with the commercial UR5e as a case. The new dynamic map is based on a physical interpretation of the robot arm, followed by strategic simplification. The new map of the vibration modes can be described by only 10 identified coefficients. Additionally, FD-TVIST is extended to the multi-mode case. The combination of new methods yields an efficient vibration suppression featuring short time delay, great robustness, simple implementation, low-cost computation, and insensitivity to trajectory generation method. Experimental implementation and validation in a commercial UR robot show that the residual vibration of the robot manipulator is reduced up to 90% with the developed vibration control method.

© 2020 Elsevier Ltd. All rights reserved.

1. Introduction

The latest development in robot arm designs shows a trend in lightweight design. This is particularly true for the collaborative robots (cobots). A cobot is a *robot designed for direct interaction with a human* [1], and the relatively new field is one of the fastest growing sectors within robotics [2]. Lightweight structural design enables a high safety level due to reduced impact in a potential collision with a human or an obstacle. Other motivators for lightweight design include increased operating speed, reduced cost, and reduced energy consumption, which becomes increasingly more important with more battery operated mobile robots.

However, the robot design is a compromise between low mass and high rigidity. As a consequence, lightweight robot manipulators feature increased mechanical flexibility, compared to the traditional heavy and rigid industrial robots. Mechanical flexibility can be illustrated with the UR5e robot, a collaborative robot manipulator with a lightweight design from Universal Robots A/S in Fig. 1.

Robot manipulators with mechanical flexibility exhibit non-ignorable mechanical vibrations during rapid point-to-point motions.
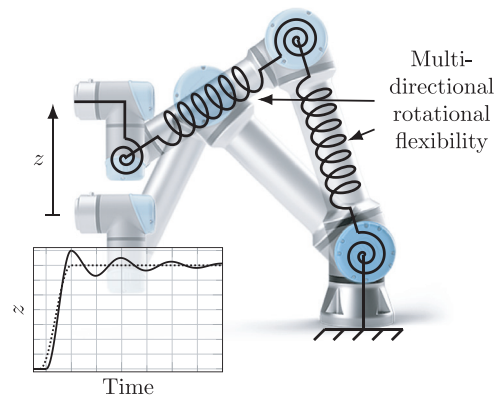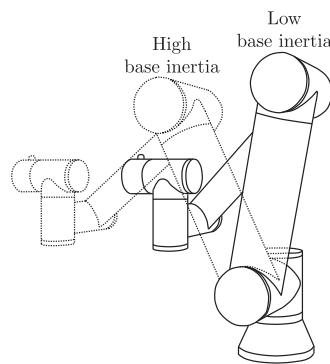

Fig. 1. Visualization of mechanical flexibility in UR5e robot.

Fig. 2. Configuration-dependent mass moment of inertia of UR5e robot.

The flexibility is located mainly in the joint gears consisting of strain wave gears, and in the links consisting of aluminum tubes. Joints and links have longitudinal and rotational flexibility. However, longitudinal flexibility is negligible in terms of mechanical vibrations. The end-effector oscillations are governed by flexural deformation of the joints and links.

Therefore, significant amount of efforts have been made towards developing vibration suppression methods for robot manipulators with flexible components [3–6].

Input shaping technology is one of the vibration suppression methods that have been received a large amount of attention [7,8]. It is attractive because it can offer efficient vibration suppression with a short time-delay, if accurate estimates of the natural frequency and damping are available for the controlled system. It has been proven, that input shaping filters can always be of shorter duration than digital low-pass or notch filters with similar vibration suppression capability [9]. Shorter filter duration yields a more responsive system, which provides higher productivity, thereby making input shaping appealing in robotics.

By input shaping, the original (unshaped) system input is convolved with a set of well-designed impulses to generate a new (shaped) system input [10]. The timing and magnitudes of the impulses are designed based on the natural frequencies and damping ratios of the system, so that the shaped input will suppress vibrations.

However, the original input shaping method can not efficiently suppress vibrations of industrial robot arms. This is primarily because industrial robot arms exhibit configuration-dependent mass distribution, as illustrated in Fig. 2, and therefore configuration-dependent dynamic response. Here, the configuration refers to the robot pose and payload. The robot configuration varies over time, thus natural frequency(s) and damping ratio(s) are varying over time. Therefore, the robot is said to have time-varying dynamics.

Advanced dynamic models can be used for offline planning by numerical simulations and iterative procedures [11]. An approach to online planning is Time-Varying Input Shaping Technology (TVIST).

TVIST has been developed for systems with time-varying dynamics. These methods are divided into continuous time (symbolic) TVIST and discrete time (digital filter) TVIST methods. The continuous time TVIST feature good vibration suppression, but lacks freedom in practical applications, because a symbolic description of the trajectory must always be known for some time ahead. Chang and Park implemented continuous time TVIST in an industrial robot with promising results [12]. They estimated one vibration mode around the base joint, based on the horizontal payload radius. Chatlatanagulchai et al. suggested a segmentation approach to continuous TVIST and only updated the estimated dynamics in intervals [13]. Kivila

implemented continuous TVIST in a prototype robot with highly flexible links with limited success due to modeling errors [14].

More practical freedom in trajectory generation can be achieved by discrete time TVIST, where the discrete time unshaped motion is simply filtered by a digital filter to produce a discrete time shaped motion. However, discrete time TVIST introduce numerical noise, which introduce vibrations in the system. This issue is addressed by multiple researchers to tackle the challenge. Magee and Book suggested modified command shaping to forget or remember impulses between time steps [15], Rappole suggested linear impulse splitting [16], Murphy and Watanabe suggested a more advanced impulse splitting method with damping taken into account [17]. These methods definitely reduce the numerical noise, but does not eliminate it to an acceptable level, when shaping position signals [18].

Recently, a new approach to discrete time TVIST, namely Fractional Delay TVIST (FD-TVIST), was presented based on Fractional Delay FIR filtering in our preliminary work [18]. FD-TVIST eliminate the numerical issues and enable discrete time TVIST as a practical TVIST method for industry. The method is thoroughly analyzed, and verified by numerical simulations. Our later work presented preliminary experimental results conducted on a UR5e robot [19]. The preliminary results verified the working principle of FD-TVIST and showed promising vibration suppression capability with an overly simplified single mode estimate of the dynamic response characteristics.

A robot arm is a continuously distributed dynamic system with a theoretically infinite number of vibration modes. However, it is well known, that most robot arms have two dominating modes around the base and shoulder joints, respectively [20]. This is also observed, for the UR5e robot. While time-invariant multi-mode input shaping can be achieved simply by cascading multiple shaping filters, this is not possible for multiple FD-TVIST filters because the reference configuration used for estimating multiple vibration modes must be synchronized in time. Therefore, this paper presents a new method for extending of FD-TVIST to Multi-Mode vibrations.

TVIST requires a reliable and accurate estimate of the system dynamics in real time. It is well known that it is challenging to achieve an accurate estimate of the dynamics [21–23]. Kivila estimated 3 vibration modes by a Transfer Matrix Method (TMM) [14]. He found that the suggested estimator was too inaccurate for TVIST and too computationally expensive for real time applications. He states in future work, that this should be improved.

Kim and Croft recently stated [20]: *However, realization of ($\omega_n(\vec{q}, t)$, red.) is extremely difficult in practice for industrial robots due to their complex dynamics. The modes vary significantly depending upon the robot's position.*

Advanced models such as finite element analysis with accurate 3D CAD models can be employed to model the non-linear dynamics of an industrial robot [24]. However, it can be difficult to obtain all relevant parameters from a CAD model, such as joint friction and stiffness parameters, and therefore experimental identification of the assembled robot appear to be the only practical approach for an accurate model [25]. Advanced identification methods have been presented based on multivariable frequency response functions. For example the 18DOF extended flexible joint model presented by Moberg et al. for an industrial 6DOF robot [26]. This is an accurate model for a complete robot arm. Many complex and coupled vibration modes are captured by the model.

However, the most accurate models, such as 3D CAD models or multi-variable frequency response functions, is not necessarily the best basis for efficient input shaping. Input shaping is fundamentally assuming the system to have a linear dynamic response [7]. Therefore, the best input shaping results will be achieved with a linear model. Also, it is challenging to distinguish different vibration modes from each other based on the frequency response function.

To the best knowledge of the authors, no estimator has been designed specifically for input shaping performance. The estimator needs to be accurate enough, while also simple enough for a real time estimator running for example 500 Hz, like the UR5e controller.

In order to provide the best basis for efficient input shaping, this paper presents a new estimation method, which is specifically developed for multi-mode time-varying input shaping. The new method is based on a heuristic system approach, and treats the system as linear time-varying in order to respect the input shaping method. Two vibration modes are individually modeled.

An estimate could be obtained by interpolating over a lookup table of measured properties. A set of interpolation variables must be chosen. Variables, which affect the system dynamic response, include joint positions (except the base joint), payload mass, payload center of gravity, and payload inertia matrix. Even if payload inertia matrix is neglected, this amounts to $5 + 1 + 3 = 9$ variables. Assuming that a 3rd order multi-variate polynomial is appropriate, the interpolation requires $\binom{9+3}{9} = 220$ coefficients for each interpolated value [27]. Thus, for two natural frequencies and two damping ratios, 880 coefficients are required. Also, it can be dangerous to blindly make a polynomial interpolation. The estimate can be dramatically wrong outside the tested scenarios, and the large number of variables makes it challenging to interpret the nature of the resulting function.

However, the vibrational properties of a robot arm follows basic physical rules, related to mass and flexibility distribution, as Hoevenaars et al. exploit for the parallel manipulator [28]. The mass distribution, i.e. mass moment of inertia on different joint axes, can be determined by basic forward kinematics. The major vibrational characteristics are related to the mass moment of inertia around base and shoulder joints.

This paper presents a method for estimating the configuration dependent dynamics of a robot arm by only 10 coefficients and 2 variables. In order to meet the requirement of a real time vibrational characteristics estimator for Multi-Mode FD-
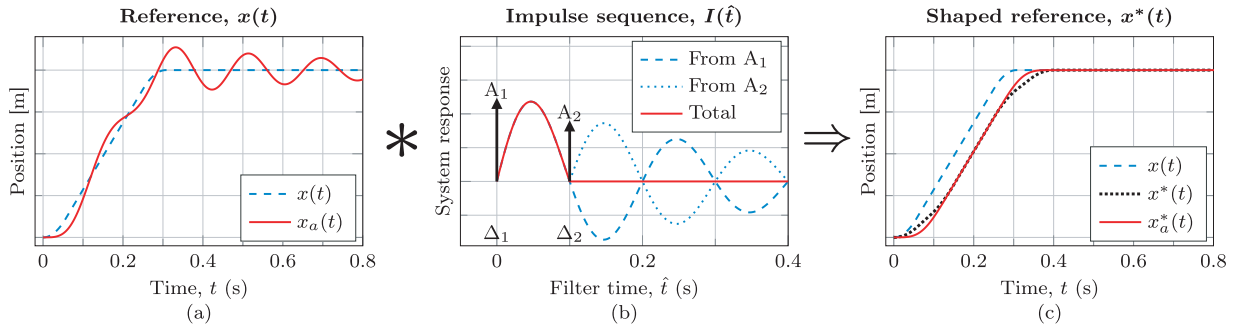
Fig. 3. The input shaping principle.

TVIST, this paper presents a new toolbox for establishing a real-time estimator for the two dominant vibration modes of a robot arm with the UR5e as a case study. The toolbox includes 1) a new physically sound symbolic map, of the dominant natural frequencies and damping ratios, which is simple enough to evaluate within the existing control hardware 2) a new practical identification method for vibrational characteristics of a robot with an accelerometer at the tool flange, and 3) a new practical and automatic mapping method for identification of the dynamic map coefficients.

The rest of this paper is organized follows: First, we formulate and define the overall problem in Section 2. Second, we present the new Multi-Mode FD-TVIST method and implementation in Section 3. Third, we systematically elaborate the principle and procedure of the novel multi-mode dynamic mapping method in Section 4. Fourth, we validate the dynamic mapping with experimental results in Section 5. Fifth, we conduct the experimental testing on a UR5e robot to validate the proposed vibration control method with experimental results using multi-mode FD-TVIST through the dynamic mapping in Section 6. Finally, we conclude this work in Section 7.

2. Problem formulation

The problem, which this paper aims to handle, is the residual vibration suppression of lightweight robot manipulators using a UR robot as a case study. The unwanted mechanical vibration of lightweight robot manipulators is not negligible when conducting high-speed rest-to-rest operation manipulations. In order to increase the productivity and applicability of light weight robots, it is sought to reduce the amount of residual vibrations. The input shaping technology is employed as the method to reduce the vibration because of its well-approved efficiency and effectiveness. To implement input shaping technology on industrial robot manipulators, the natural frequencies and damping ratios need to be estimated online in real time. The experimental implementation face challenging issues: complex nonlinear, multi-mode, and time-varying dynamic responses. To solve this challenging problem, the complex dynamics of the robot manipulator need to simplified into linear dynamics with dominant modes. Then, a practical and efficient dynamic mapping method needs to be developed to perform the estimate of time-varying natural frequencies and damping ratios. Finally, a multi-mode TVIST needs to be proposed and experimentally implemented on the industrial robot manipulator. The challenging problem is divided into the following sub-problems:

- Formulate a Multi-Mode TVIST method with application to industrial robots
- Develop a practical multi-mode dynamic mapping method for UR robots
- Identify and validate dynamic map
- Validate the performance of Multi-Mode TVIST with the dynamic map by implementation in a UR robot

The next subsection presents the principles of input shaping and the extension of FD-TVIST to Multi-Mode vibrations.

3. Input shaping

Input shaping is a vibration suppression method, that modifies the reference signal for a dynamic system, such that it will avoid to introduce unwanted oscillations in the system. Input shaping is purely feed-forward and does not affect vibrations from external disturbances. The method is based on the posicast principle, i.e. that an impulse will yield a dynamic response in the system and thus it is also possible to introduce a second impulse, which cancels out the response of the first impulse. This is possible, if the second impulse has the right amplitude and timing.

The posicast principle is visualized in Fig. 3b.

Here it is seen, how an impulse with timing Δ_1 and magnitude A_1 will introduce a dynamic response in the system. It is also seen, that an impulse with timing Δ_2 and magnitude A_2 can be designed, such that the resulting response will cancel out the response of the first impulse.

However, reference signals for robots consist typically from a reference position, possibly in conjunction with other reference signals such as reference velocity, reference torque, etc. Thus it is necessary to modify these reference signals, such that they will not introduce vibrations in the system.

Such an original (unshaped) reference position, $x(t)$, is illustrated in Fig. 3a together with the corresponding actual position, $x_a(t)$. It is seen, that $x_a(t)$ has a dynamic response to $x(t)$.

If a vibration free impulse sequence, $I(\hat{t})$, is known for the system, such as the sequence illustrated in Fig. 3b, it is possible to modify $x(t)$ by convolving it with $I(\hat{t})$ as illustrated in Fig. 3c, and thereby obtain a new (shaped) reference position, $x^*(t)$, which will not introduce vibrations in the system. The resulting actual position from the shaped reference, $x_a^*(t)$ has no residual vibrations.

The next subsections presents an overview of the input shaping method and extends it to time-varying input shaping. Finally the practical implementation of such methods in a UR5e robot is presented.

3.1. Basics of input shaping

The corner stone of input shaping is the vibration free impulse sequence. An impulse sequence, $I(\hat{t})$, can be described as:

$$I(\hat{t}) = \begin{cases} A_i & \text{if } \hat{t} = \Delta_i \\ 0 & \text{otherwise} \end{cases} \tag{1}$$

where $\hat{t}$ is internal filter time, A_i is the amplitude of impulse i, and Δ_i is timing (or delay) of impulse i. Here i is an index in the range $\{1, \cdots, N\}$, and N is the number of impulses.

Vibration free impulse sequences with different number of impulses can be established in many different ways [29,30]. The simplest and most widely used method is called a 2-impulse Zero Vibration (ZV) impulse sequence [7]. The 2-impulse ZV filter is presented here for completeness, but it could be chosen differently. $\vec{A}$ and $\vec{\Delta}$ are computed as:

$$K = e^{\frac{\zeta \pi}{\sqrt{1-\zeta^2}}} \tag{2}$$

$$\vec{A} = \left\{ \frac{1}{1+K} \quad \frac{K}{1+K} \right\} \tag{3}$$

$$\vec{\Delta} = \left\{ 0 \quad \frac{\pi}{\omega_n \sqrt{1-\zeta^2}} \right\} \tag{4}$$

where ω_n is the (angular) natural frequency of the system, ζ is the system damping ratio, and K is a helping constant. Once $\vec{A}$ and $\vec{\Delta}$ have been established, the shaping procedure can be performed as:

$$x^*(t) = (x * I)(t) = x(t) * I(\hat{t}) \equiv \sum_{i=1}^{N} (A_i \cdot x(t - \Delta_i)) \tag{5}$$

where $I(\hat{t})$ is the impulse sequence, $*$ is the convolution operator, and $x^*(t)$ is the shaped reference, which ideally will introduce zero vibration in the controlled system. The next subsection presents the extension from input shaping to time-varying input shaping.

3.2. Time-varying input shaping technology (TVIST)

A robot arm such as the UR5e robot has time-varying dynamics, as elaborated in the introduction. Thus there is a demand to extend the input shaping method to handle time-varying dynamics. This can be achieved by allowing $I(\hat{t})$ in (1) to be time-varying, like [18]:

$$I(\hat{t}, t) = \begin{cases} A_i(\zeta(t)) & \text{if } \hat{t} = \Delta_i(\omega_n(t), \zeta(t)) \\ 0 & \text{otherwise} \end{cases} \tag{6}$$

where t is global time, and $\hat{t}$ is the local time inside the filter. It is seen, how the local impulse sequence $I(\hat{t})$ can now vary with t. By including (6) in (5), the shaped reference from time-varying input shaping becomes:

$$x^*(t) = \sum_{i=1}^{N} \left(A_i(\zeta(t)) \cdot x\left(t - \Delta_i(\omega_n(t), \zeta(t)) \right) \right) \tag{7}$$

The next subsection presents the discrete time implementation of TVIST in the UR5e robot.

3.3. TVIST Implementation

The idealized description of time-varying input shaping in (7) must be designed into a real-time implementation, which can be implemented in the robot control structure. This can be achieved in continuous time [12] or discrete time domain [18]. The choice of time domain depends on the existing system, in which it is desired to integrate TVIST.
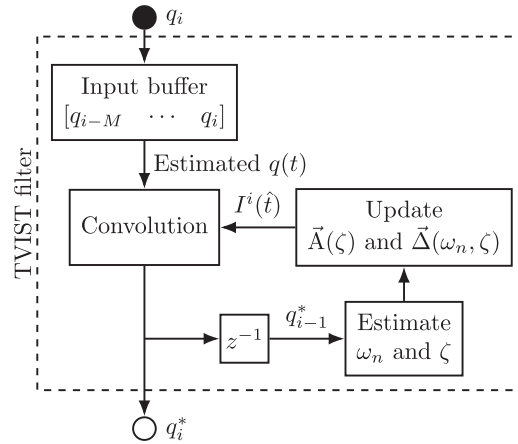
Fig. 4. Discrete time implementation of TVIST.

For the UR control structure, it is desired to implement a discrete time TVIST filter. The choice of filter architecture is based on the Fractional Delay Finite Impulse Response filter (FD-FIR), and the system dynamics are estimated based on the latest shaped joint positions, like [19]. More details on the FD-TVIST discrete time implementation are presented in our earlier work with theoretical proofs, detailed analysis, numerical simulations, and comparison with other discretization strategies [18].

The filter architecture is illustrated in Fig. 4, where q_i is original joint reference position at time step i, q_i^* is the shaped joint reference position, and z^{-1} denotes a discrete time delay of one time step.

The input buffer holds the latest $M + 1$ values of q. Here, M must be sufficiently large, such that $q(t - \triangle_N)$ can be estimated. The value of $\triangle_N$ will vary for time-varying input shaping. In practice, the amount of data in the buffer is very small for modern computers, and is not an issue. Therefore, it is suggested to fix the buffer length based on the maximum possible value of $\triangle_N$ for the specific system and choice of impulse scheme as $M = SF \times \triangle_N^{\max}/dt$, where dt is the discrete time step and $SF \approx 1.5$ is a safety factor. It is suggested to implement the buffer as a circular buffer to reduce processing [31].

The presented filter structure is for vibration suppression of a single vibration mode. The next subsection presents an extended architecture for multi-mode vibration suppression.

3.4. Multi-mode TVIST implementation

For the UR5e robot, it is observed, that two vibration modes will be governing the dynamic response of motions. This observation is presented in detail in Section 4.1. Thus it is desired to implement a two-mode TVIST in the robot, in order to avoid introducing vibrations in either vibration mode.

Previous research has been focused on either multi-mode input shaping or time-varying input shaping. Thus, multi-mode TVIST has not been presented before. Whereas non-varying multi-mode input shaping can be obtained simply by chaining multiple filters in series [32–34], this is not optimal for multi-mode time-varying input shaping. This is because time-varying filters need to be updated like illustrated in Fig. 4. If these filters are blindly chained, they will be updated based on different reference positions, which will deviate to a varying degree from the actual configuration of the robot.

Therefore, it is suggested to follow the illustrated structure in Fig. 5.

Here it is seen how individual TVIST filters are simply cascaded, except from one important detail: The estimated ω_n and ζ for each vibration mode are updated based on the same configuration, namely the previous output from the last filter in the chain, q_{i-1}^{**}. Thereby all vibration modes are estimated based on the q_{i-1}^{**}, which is deemed close to the actual position of the robot. The structure of Fig. 5 can easily be extended to an arbitrary number of vibration modes.

The presented method is purely feed-forward, and do not depend on sensor measurements. Thus, the filter is not sensitive to measurement noise. Instead the filter depends on a method for estimating the system dynamics for a specified robot configuration. The next section discloses a new method of dynamic mapping, which enables such an estimate.

4. Dynamic mapping of UR5e robot

A successful TVIST implementation depends on a reliable estimate of the natural frequencies and damping ratios of the system. This section presents a method for estimating the UR5e dynamics by dynamic mapping. The outcome is a map of ω_n and ζ for two observed vibration modes in the robot.
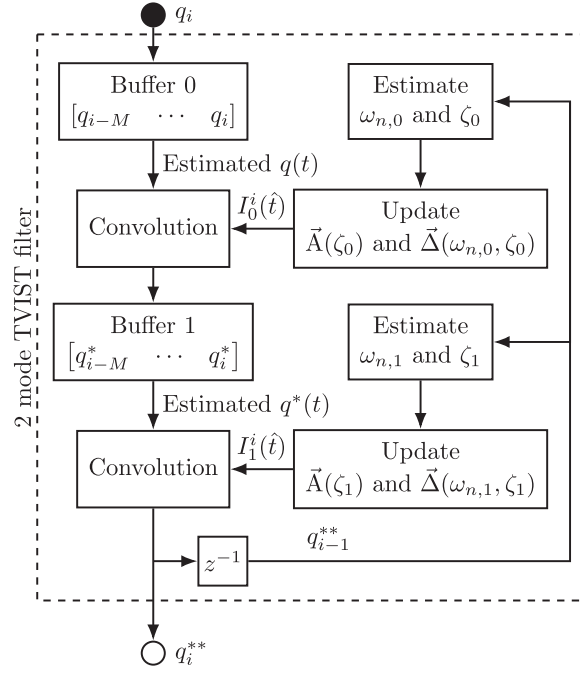
Fig. 5. Discrete time implementation of multi-mode TVIST.
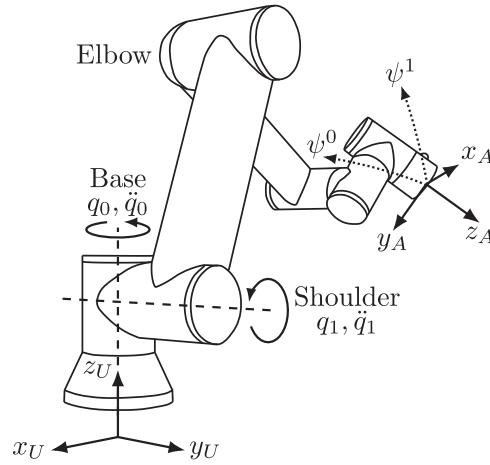

Fig. 6. Expected vibration modes of a UR5e robot.

4.1. Observed vibration modes

Complicated vibration modes are expected, when examining the structure of a UR5e robot in an arbitrary configuration. The complicated dynamic system with continuously distributed mass, flexibility, and damping will be subject to a multitude of different vibration modes in all directions.

However, it is assumed that mechanical flexibility can be approximated as rotational flexibility in the joints, such that link flexibility is concatenated into the joint flexibility, resulting in an equivalent torsional stiffness. Attention should be drawn to the joints, that are closest to the base of the robot.

There are three reasons, that the joints near the base have a large impact on the dynamic behavior: 1) Because an angular deflection near the base will result in large tool displacement, whereas an angular deflection in the wrist of the robot will only result in minor tool displacement, 2) Because the joints near the base experience higher inertia, and thereby lower natural frequencies, and 3) Because the joints near the base experience higher load torques.

Based on these observations, it is expected that UR5e robot will have its most dominant vibration modes as rotational modes around the base joint and shoulder joint. Base and shoulder joints are illustrated in Fig. 6.
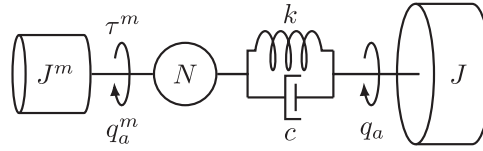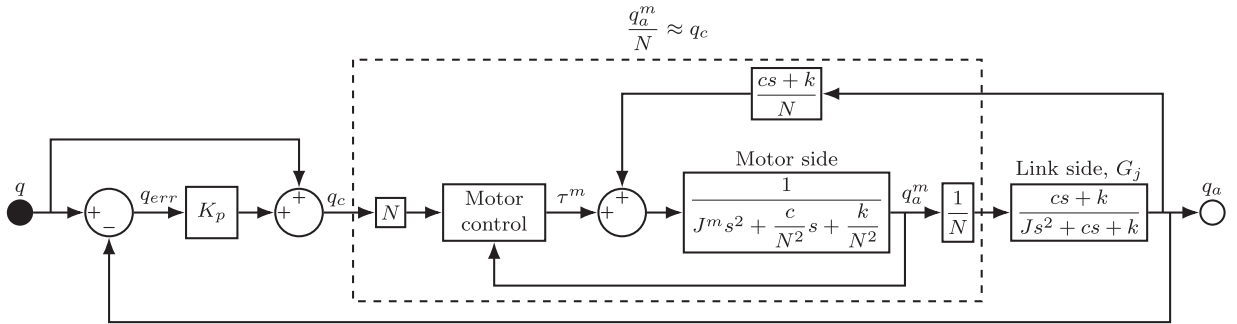
Fig. 7. Joint mechanical dynamics.

Fig. 8. Joint control structure.

It can be discussed, whether vibrations around the elbow joint should also be considered an individual vibration mode. However, the joint axes of shoulder and elbow are always parallel. Thus it is expected that the flexibility of the elbow joint can be reflected in the shoulder joint as one equivalent torsional stiffness. The flexibility of the wrist joints does influence the system dynamics, and can not be ignored [26]. In this work, it is assumed that flexibility of wrist joints can also be reflected on the base and shoulder joints.

To conclude, it is assumed that vibrations of the UR5e robot can be approximated by two vibration modes: 1) around the base joint, and 2) around the shoulder joint. The next section will elaborate on the expected configuration-dependency of the natural frequency and damping of the two vibration modes.

4.2. Configuration dependent dynamics

It is known, that a typical industrial robot arm with 6 degrees of freedom (DOF) has configuration-dependent dynamic behavior. In other words, the robot is a complicated non-linear dynamic system. The fundamentals of input shaping methods relies on assumptions of linear dynamic response [7]. This estimator is developed specifically for effective vibration suppression by input shaping. Therefore, it is essential to approximate the system to be locally linear, when the estimate is to be used for input shaping. This can be counter-intuitive, because more accurate non-linear models can be developed, but the linear model will yield superior performance of input shaping. Cho and Park [35] state accurately: *Flexible multibody systems undergoing a large rigid body motion tend to appear like linear time-varying systems in the sense of natural frequency shifts. Such examples can be found in many areas, especially in robotics.* Thus, it is assumed, that a time-varying linear model will be a good estimator, and provide a good basis for time-varying input shaping.

In a 6DOF robot arm, there are multiple contributions to the configuration-dependent behavior. Contributions include variations in payload, mass distribution, and control parameters, non-linear stiffness of gears and load-dependent friction, etc.

Among these factors, it is expected, that mass distribution (system inertia) has the largest impact on configuration dependency of natural frequencies and damping. Chang and Park showed a near linear relationship between natural frequency around the base joint and horizontal distance to payload [12]. In this paper, the robot will be treated as a more nuanced configuration-dependent dynamic system with multiple physical time-varying behaviors taken into account.

4.3. System dynamics

The mechanical joint dynamics are modeled as illustrated in Fig. 7, where J^m is motor inertia, τ^m is motor torque, q_a^m is actual motor side joint angle, N is gear ratio, k is gear stiffness, c is gear viscous damping, q_a is actual link side joint angle, and J is the link side inertia.

Conceptually, the control structure can be presented as a combination of link side and motor side control, like illustrated in Fig. 8, where q is the reference link side joint angle. A link side position control loop defines a reference control position q_c. It is assumed that this controller is a type of PID controller. However, this increases the order of the closed loop dynamic system. It is consistently sought to keep the system as a 2nd order system, in order to provide the best basis for input
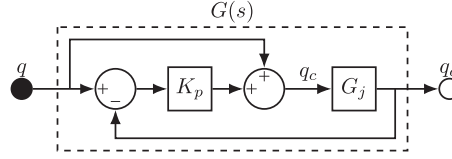
Fig. 9. Closed loop joint dynamics.

shaping. Thus, it is assumed that the governing dynamics of the link side control loop can be approximated by a proportional controller, i.e. P control with gain K_p, which does not impact the order of the closed loop system.

An inner feedback loop controls q_a^m. It is assumed, that this motor side control is rigid enough, that $q_a^m/N \approx q_c$, as proven for other controllers [20]. Thereby, the closed loop dynamics can be simplified as illustrated in Fig. 9, where G_j is the link side joint dynamics transfer function:

$$G_j(s) = \frac{\mathcal{L}\{q_a\}}{\mathcal{L}\{q_a^m/N\}} = \frac{cs + k}{Js^2 + cs + k} \tag{8}$$

and $G(s)$ is the closed loop system transfer function. The closed loop system transfer function can be found from Fig. 9 by the signal-flow graph method [36] as:

$$G(s) = \frac{\mathcal{L}\{q_a\}}{\mathcal{L}\{q\}} \tag{9}$$

$$= \frac{(1 + K_p)\, G_j(s)}{1 + K_p G_j(s)} \tag{10}$$

$$= \frac{cs + k}{\frac{J}{1+K_p}s^2 + cs + k} \tag{11}$$

Notice, that $G(s)$ reduces to $G_j(s)$ for a system without link side feedback control, i.e. $K_p = 0$.

4.4. Estimating dynamics from accelerometer data

There are multiple ways to estimate the vibrational parameters of a robot. It requires a source of excitation, such as reference actuator current [37], reference actuator speed [26], or a hit by an impact hammer [38]. It also requires sensor data for quantifying the vibration, such as motor position encoder [26], joint torque sensor [37], or accelerometer [26,38].

For example, it is possible to analyze both motor and link side of each joint. However, the ultimate goal is not to avoid joint oscillations, but to eliminate tool oscillations. Therefore, it is chosen to utilize one of the unique features of the UR robots, namely the built-in accelerometer in the tool flange. Data from the target motion together with sensor data, such as accelerometer readings, are easily available from the Real-Time Data Exchange interface of the robot. By analyzing the dynamics between target joint motion and actual tool motion, it is possible to capture all components of the dynamic system, including link flexibility, and potential impact from a flexible robot mounting. These effects are otherwise not captured. Basically, target joint acceleration yields tool acceleration. Therefore, it is necessary to determine the dynamic behavior of the complete chain of elements connecting the two.

The natural frequency can for example be determined from a frequency response function [26,39]. The frequency response function can provide a very nuanced description of the dynamic behavior of the system at different excitation frequencies, and for example reveal multiple resonance frequencies. However, input shaping can not utilize this detailed information. Input shaping needs the single set of natural frequency and damping ratio of a linear 2nd order system, which can best approximate the physical system. This can be achieved by fitting a 2nd order transfer function to the recorded data for target joint acceleration and actual tool acceleration.

This section presents a detailed procedure for estimating the dynamics in a specific configuration of the robot by fitting target joint acceleration, and tool accelerometer readings to a 2nd order transfer function. Here, A denotes the local accelerometer coordinate frame, illustrated in Fig. 6.

4.4.1. Gravity and orientation compensation

Some post processing of the accelerometer measurements are needed before they can be used in dynamics estimation. Here it is desired to obtain an acceleration signal $^U\vec{\psi}$, which is expressed in the universal coordinate frame, U, illustrated in Fig. 6, and without gravity [40–43]:

$$^U\vec{\psi} = {}_A^U R {}^A\hat{\vec{\psi}} - \begin{pmatrix} 0 & 0 & g \end{pmatrix}^T \tag{12}$$

where $^A\hat{\vec{\psi}}$ is the raw accelerometer measurements in accelerometer frame (A), $^U_A R$ is the rotation matrix of frame A relative to U, and g is the acceleration of gravity, ~ 9.82 m/s². In practice, the direction and magnitude of gravity is determined as the average value of the acceleration vector, $^U_A R {}^A\hat{\vec{\psi}}$, at short a period of standstill, e.g. 10 samples.
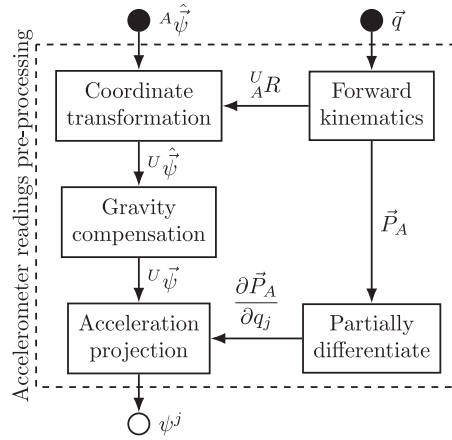
Fig. 10. Accelerometer reading pre-processing to obtain tangential acceleration.

4.4.2. Tangential acceleration

If only one joint is moving, and mechanical flexibility is neglected, there is a linear relation between angular acceleration in the joint, $\ddot{q}_j$, and tangential acceleration, ψ^j, which is illustrated in Fig. 6. This makes ψ^j a very interesting measure, because it allows for a lot of simplification, when estimating system dynamics.

Contributions from centrifugal or Coriolis accelerations can be disregarded by looking at the tangential acceleration instead of the magnitude of acceleration. This is desired, because centrifugal and Coriolis accelerations are results of joint velocity, $\dot{q}_j$ and not joint acceleration, $\ddot{q}_j$. The tangential acceleration can be found as:

$$\psi^j = \frac{{}^U\vec{\psi} \cdot \frac{\partial \vec{P}_A}{\partial q_j}}{\left| \frac{\partial \vec{P}_A}{\partial q_j} \right|} \tag{13}$$

where ${}^U\vec{\psi}$ is the gravity compensated accelerometer reading in the universal coordinate frame, and $\frac{\partial \vec{P}_A}{\partial q_j}$ is the partial derivative of the accelerometer position, $\vec{P}_A$, with respect to joint angle, q_j. $\frac{\partial \vec{P}_A}{\partial q_j}$ is the tangential direction of interest, and the acceleration component in the tangential direction is found by a scalar projection. $\frac{\partial \vec{P}_A}{\partial q_j}$, is also the jth column of the 6×6 Jacobian matrix [42]. This can be a time-consuming process to derive, but it can be approximated numerically by infinitesimal motions.

Thereby, the tangential acceleration has been obtained by pre-processing the raw accelerometer readings based on the joint angles. An overview of the pre-processing procedure is presented in Fig. 10.

The next subsection explains how to obtain the natural frequency and damping ratio by fitting the pre-processed measurements to a transfer function.

4.4.3. Modeled tool acceleration

The robot can be thought of as a single link manipulator, when moving only one joint. Without loss of generalization, the accelerometer position, $\vec{P}_A$, will move on a circular arc, when moving only one joint. When assuming flexible joints and rigid links, there will be a linear relationship between actual joint acceleration, $\ddot{q}_a$, and the tangential acceleration of the accelerometer, ψ^j [44]:

$$\psi^j = r\ddot{q}_a \tag{14}$$

where radius r is the distance from joint axis to accelerometer position. Thereby, a transfer function relationship, $G_a(s)$, can be established between target joint acceleration and actual tool acceleration:

$$G_a(s) = \frac{\mathcal{L}\{\psi^j\}}{\mathcal{L}\{\ddot{q}\}} = \frac{r\mathcal{L}\{\ddot{q}_a\}}{\mathcal{L}\{\ddot{q}\}} = \frac{r\mathcal{L}\{q_a\}s^2}{\mathcal{L}\{q\}s^2} = rG(s) = \frac{r\left(1+K_p\right)\left(\frac{k}{J} + \frac{c}{J}s\right)}{s^2 + \underbrace{(1+K_p)\frac{c}{J}}_{2\zeta\omega_n}s + \underbrace{(1+K_p)\frac{k}{J}}_{\omega_n^2}} \tag{16}$$

where (16) has been reorganized compared to (11), such that natural frequency, ω_n, and damping ratio, ζ, can be easily determined from the denominator.
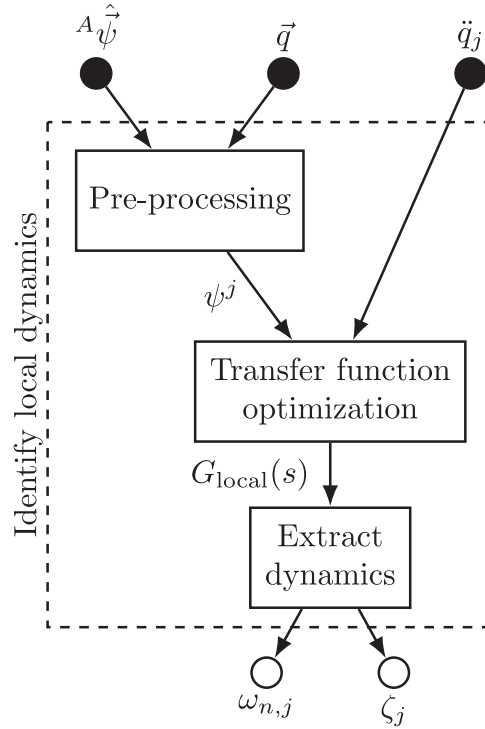
Fig. 11. Identification procedure for local dynamics.

4.4.4. Fitting to a transfer function

It is a goal to identify the local dynamics in multiple robot configurations. From $G_a(s)$ in (16) it is observed, that the transfer function has two poles and one zero. Therefore, the local transfer function is:

$$G_{\text{local}}(s) = \frac{k_a s + k_b}{s^2 + \underbrace{k_c}_{2\zeta\omega_n} s + \underbrace{k_d}_{\omega_n^2}} \tag{17}$$

where k_a, k_b, k_c, and k_d are coefficients subject to optimization.

The input shaping method relies on information about the system dynamic response in the form of natural frequency, ω_n, and damping ratio ζ, as seen from (2)–(4). Therefore, it is essential to obtain this information from the transfer function, $G_a(s)$. The dynamic response is governed by the denominator of the transfer function, and can be obtained by comparing to the characteristic second order transfer function [36]. The local natural frequency and damping can be determined from $G_{\text{local}}(s)$ in (17) as:

$$\omega_n = \sqrt{k_d}\zeta = \frac{k_c}{2\sqrt{k_d}} \tag{19}$$

Thus it is desired to obtain the parameters of $G_{\text{local}}(s)$, which are suitable for the robot in the specific local configuration. The optimization problem of optimizing $G_{\text{local}}(s)$ in (17) can be solved with the objective to minimize the model prediction error norm of the model, i.e. $|\psi^j_{\text{predicted}} - \psi^j_{\text{measured}}|$. This can be obtained by most known optimization algorithms.

To summarize the local dynamics identification procedure, Fig. 11 illustrates how to obtain ω_n, j and ζ_j from the raw accelerometer readings, $^A\hat{\vec{\psi}}$, the target joint angles, $\vec{q}$, and the target joint accelerations.

The next subsection elaborates on a description of the configuration dependent dynamic behavior.

4.5. Dynamic response map formulation

If the local system dynamics have been determined for a sufficiently large number of configurations over the whole workspace of the robot, it will be possible to identify some description of the relationship between robot configuration and dynamics.

An early TVIST implementation show a relationship between base natural frequency and horizontal payload radius [12]. It would be possible to employ machine learning algorithms to determine a relationship of dynamic response related to
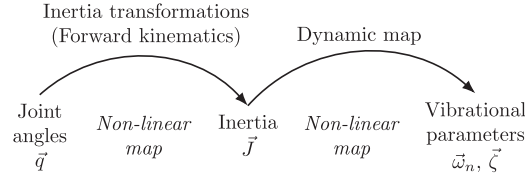
Fig. 12. Mapping from joint angles to vibrational parameters via mass moments of inertia.

payload inertia matrix, and joint angles. However, this would produce black box description with around 10 input arguments, which will be challenging to verify, and even more challenging to certify in terms of safety.

Instead, it is desired to employ system knowledge to derive a parametric description, which makes physical sense in accordance with the understanding of the dynamic system, $G_a(s)$.

Thus, the natural frequency and damping is derived from $G_a(s)$ by comparing to the characteristic transfer function. The natural frequency, ω_n, and damping ratio, ζ, can be obtained by:

$$\omega_n = \sqrt{1 + K_p}\,\sqrt{k/J} \tag{20}$$

$$\zeta = \frac{\sqrt{1 + K_p}\,c}{2\sqrt{kJ}} \tag{21}$$

It is realized from (20) and (21), that ω_n and ζ are varying with the mass moment of inertia, J. Mechanically, the dynamic response depend on inertia variations, not joint angles. This observation allows for a physically sound dynamic map based on mechanical analysis and simplifications, instead of learning algorithms.

The mass moment of inertia, experienced on each joint axis in a local configuration can be determined by standard procedures for forward kinematics and inertia transformations from joint angles [42]. Note, that it is necessary to know the inertia tensor of each movable part, including the payload, in order to perform the inertia transformation.

With this in place, it is seen, that the dynamics can be estimated from mass moments of inertia, which can be determined from joint angles, as visualized in Fig. 12. Here, the *dynamic map* denotes a mathematically formulated relation between mass moments of inertia and the vibrational parameters of the system.

In addition, three other contributions to configuration depended dynamics are expected; 1) a gear stiffening effect, 2) a configuration damping friction coefficient, and 3) a controller gain adaption. These phenomena will be justified and explained here.

4.5.1. System stiffness variations

First, a gear stiffening effect is expected to impact the system dynamics. Because UR robots are equipped with strain wave gears, which have a significant impact on overall impedance of the system. The torque-displacement relationship of a strain-wave gear is usually approximated as a cubic polynomial like Kim and Croft [20], Tuttle [45], Zhang et al. [46], Madsen et al. [47]:

$$\tau \approx k_1 \delta q + k_3 \delta q^3 \tag{22}$$

where τ is the joint torque, δq is angular deformation, and where k_1 and k_3 are polynomial coefficients. A torque-displacement curve for the strain wave gear of a UR5e base joint is presented in Fig. 13. The figure is generated with $k_1 = 42.0$ Nm/(rad$\times 10^{-3}$) and $k_3 = 2.4$ Nm/(rad$\times 10^{-3}$)^3, which produce a curve nearly identical to the results of Madsen et al. [47].

It is possible to describe the equivalent stiffness coefficient of the gear with (22) as:

$$k = \frac{\partial \tau}{\partial \delta q} \approx k_1 + 3k_3 \delta q^2 \tag{23}$$

which is also illustrated in Fig. 13. However, it is not straight forward to use a description in terms of displacement to approximate stiffness, because gear deformation is not known from the configuration of the robot. Thus it is desired to obtain a description in terms of torque instead, because torque is related to the configuration and mass moment of inertia. By isolating δq in (22) using Wolfram Alpha this relation is found as:

$$\delta q = \frac{\sqrt[3]{\sqrt{3}\sqrt{4k_1^3 k_3^3 + 27k_3^4 \tau^2} + 9k_3^2 \tau}}{\sqrt[3]{2}\,3^{2/3}k_3}$$

$$-\frac{\sqrt[3]{\frac{2}{3}}k_1}{\sqrt[3]{\sqrt{3}\sqrt{4k_1^3 k_3^3 + 27k_3^4 \tau^2} + 9k_3^2 \tau}} \tag{24}$$
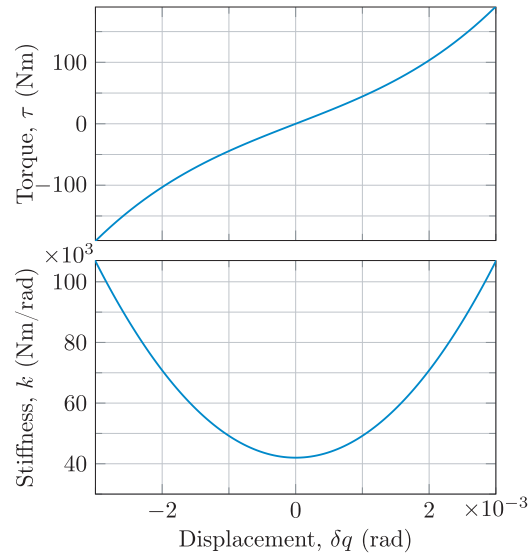
Fig. 13. Force displacement curve for strain wave gear in UR5e base joint, adjusted according to Madsen et al. [47] (top). Stiffness displacement curve for UR5e base joint (bottom).
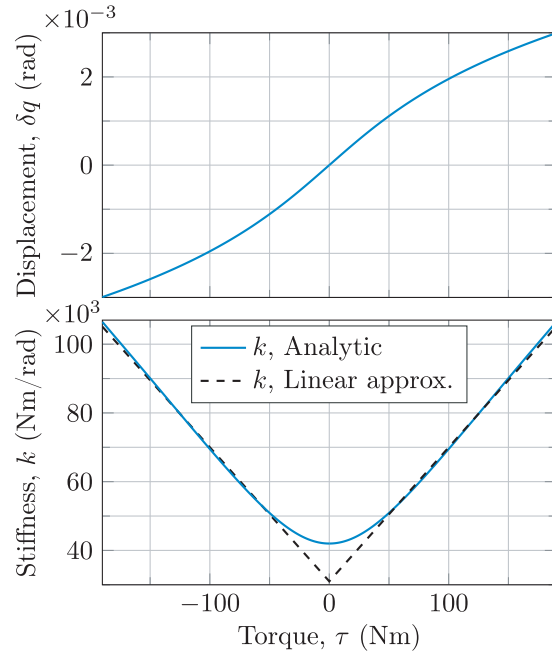
Fig. 14. Displacement force curve for strain wave gear in UR5e base joint (top). Stiffness torque curve for UR5e base joint (bottom).

which is illustrated in Fig. 14.

Then it is possible to replace δq in (23) with the expression in (24) to obtain an expression for stiffness in terms of torque. The expression will become:

$$
k \approx k_1 + 3k_3 \left(\frac{\sqrt[3]{\sqrt{3}\sqrt{4k_1^3 k_3^3 + 27k_3^4 \tau^2} + 9k_3^2 \tau}}{\sqrt[3]{2}\, 3^{2/3} k_3} - \frac{\sqrt[3]{\frac{2}{3}}k_1}{\sqrt[3]{\sqrt{3}\sqrt{4k_1^3 k_3^3 + 27k_3^4 \tau^2} + 9k_3^2 \tau}} \right)^2
\tag{25}
$$

which is illustrated in Fig. 14. From the illustration, it is visually determined, that it is acceptable to approximate (25) as partially linear, i.e. as:

$$k \approx a + b|\tau| \tag{26}$$

where a and b are the coefficients of the symmetrical linear approximation of the stiffness, k. The linear approximation is also illustrated in Fig. 14.

It is seen from the rotational Newtons second law, that torque, τ, is directly proportional with mass moment of inertia, J, if the acceleration $\ddot{q}$ is constant:

$$\tau = J\ddot{q} \tag{27}$$

$$|\tau| \propto J \tag{28}$$

Therefore, under the assumption, that joint accelerations are equivalent for different configurations, it is determined, that the robot gear stiffness variations can be approximated as:

$$k \approx a + bJ \tag{29}$$

where b also captures a proportionality factor between J and $|\tau|$.

The gravity load, i.e. the average load, should also be taken into account because this will put additional torque on the gear and thereby affect the local stiffness. It is chosen to approximate this contribution to be proportional to $|\tau_g|$, based on the stiffness curve (26) in Fig. 13. Therefore the mechanical stiffness is approximated as:

$$k \approx k_0 + k_J J + k_g |\tau_g| \tag{30}$$

where k_0 is a constant coefficient, k_J is the inertia dependency coefficient, and k_g is the gravity torque dependency coefficient. Together, these coefficients describe the stiffness variations of the strain wave gears.

Actually, the non-linear bending force-displacement relation of beams (like aluminum tube links of the robot) can also be approximated as cubic polynomial [48,49], similar to the strain wave gear. Thus, the stiffening effects of the links will also be captured by (30) without any additional effort.

4.5.2. System damping variations

Friction estimation is in general a very complex branch of research, and friction in strain-wave gears is no different. The friction torque depends for example non-linearly on velocity, load torque, position, temperature, and history [45,47,50,51]. The linear ideal 2nd order dynamic system, $G_j(s)$ in (8) has linear viscous damping:

$$\tau_{\text{damping}} = -c\dot{\delta q} \tag{31}$$

where τ_{damping} is the friction damping torque, c is the linear viscous friction coefficient, and $\dot{\delta q}$ is the gear deflection rate.

However, strain wave gears feature a multitude of friction components, of which several are non-linear, e.g. non-linear viscous friction and torque dependency [51]. Wolf and Iskandar suggest to model non-linear viscous friction of a strain wave gear as [50]:

$$\tau_{\text{viscous}} = -(c_0 \dot{q} + c_1 \text{sign}(\dot{q})\dot{q}^2 + c_2 \dot{q}^3) \tag{32}$$

$$= -\underbrace{\left(c_0 + c_1 \text{sign}(\dot{q})\dot{q} + c_2 \dot{q}^2\right)}_{c_{\text{nl}}(\dot{q})} \dot{q} \tag{33}$$

where τ_{viscous} is the non-linear viscous friction torque, $\dot{q}$ is the joint velocity, c_0, c_1, c_2 are the polynomial coefficients of non-linear viscous friction, and $c_{\text{nl}}(\dot{q})$ is the equivalent non-linear viscous friction coefficient.

It is assumed, that this type of non-linear viscous friction can also describe the friction for internal gear deformation, $\dot{\delta q}$:

$$\tau_{\text{damping-viscous}} = -\underbrace{\left(c_0 + c_1 \text{sign}(\dot{\delta q})\dot{\delta q} + c_2 \dot{\delta q}^2\right)}_{c_{\text{nl}}(\dot{\delta q})} \dot{\delta q} \tag{34}$$

It is well known, that friction increase with joint torque [52]. Here, it is assumed, that this phenomenon can be captured as a linear effect:

$$\tau_{\text{damping-load-dependent}} = -(1 + c_\tau |\tau|)c\dot{\delta q} \tag{35}$$

where τ is the joint load torque, c_τ is the torque dependent friction coefficient, and c is the linear viscous friction coefficient.

Thus, a combined load-dependent and non-linear viscous friction from (34) and (35) can be described as:

$$\tau_{\text{damping}} = -\underbrace{\left(c_0 + c_1 \text{sign}(\dot{\delta q})\dot{\delta q} + c_2 \dot{\delta q}^2\right)(1 + c_\tau |\tau|)}_{c(\dot{\delta q},\tau)} \dot{\delta q} \tag{36}$$
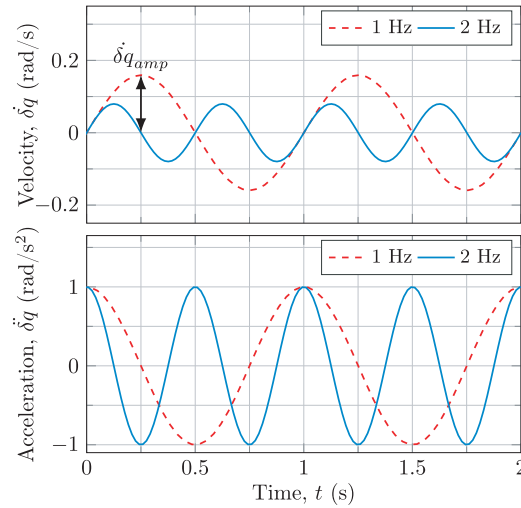
Fig. 15. Velocity variations for constant acceleration amplitudes but varying frequency.

Thereby, the damping coefficient $c(\dot{\delta q}, \tau)$ varies with both deflection rate and load torque.

It is desired to estimate damping variations based on inertia, to stay in line with the stiffness variations. It is observed, that a reduced natural frequency will lead to increased deflection rate amplitude, $\dot{\delta q}_{amp}$, as illustrated in Fig. 15. The figure illustrates how two oscillations with identical acceleration amplitudes, but different frequencies, will result in different deflection rate amplitude. The amplitude, $\dot{\delta q}_{amp}$, can be found from integration of the acceleration, $\ddot{\delta q}$:

$$\ddot{\delta q}(t) = a \cos(\omega_n t) \tag{37}$$

$$\dot{\delta q}(t) = \int \ddot{\delta q}(t)\, dt = \underbrace{\frac{a}{\omega_n}}_{\dot{\delta q}_{amp}} \sin(\omega_n t) \tag{38}$$

It is seen from (38), that the amplitude of deflection rate, $\dot{\delta q}_{amp}$, is inverse proportional to the natural frequency ω_n. It is also seen from (20), that the natural frequency, ω_n, varies with the mass moment of inertia, J, such that:

$$\dot{\delta q}_{amp} \propto \frac{1}{\omega_n} = \frac{1}{\sqrt{1 + K_p \sqrt{k/J}}} \propto \sqrt{J} \tag{39}$$

It should be stressed, that (39) is based on rough assumptions, and not strictly correct. It should be seen as an idea about the expected influence on damping, for increasing inertia, J. It is expected, that increased inertia, J, will lead to lower natural frequency, ω_n, which will lead to larger deformations, which require larger deflection rate (velocity). For estimation variations in the locally linear coefficient of friction, c, it is assumed, based on (38) and (39) that the amplitude of deflection rate, $\dot{\delta q}_{amp}$, is proportional to $\sqrt{J}$.

It is also understood, that $|\tau|$ can be seen as proportional to J (28), and that J can only take positive value, whereby c can be rewritten from (36) as:

$$c \approx \left(c_0 + c_1 \sqrt{J} + c_2 J\right)(1 + c_\tau J) \tag{40}$$

such that damping variations can also be estimated from mass moment of inertia, J. Should it turn out, that these assumptions are inappropriate or unimportant, then the parameter optimization in the identification process will yield low numerical values of c_1, c_2, and c_τ because the parameters will be non-correlated to the experimental data.

4.5.3. Closed loop controller variations

It is expected that the controller has some adaptation of gains to ensure a good performance for varying configurations. In configurations with high inertia, a high proportional gain, K_p, will lead to instability. Likewise in configurations with low inertia, a low proportional gain will provide a poor performance. It is assumed, that controller adaption can be approximated this way as:

$$K_p \approx k_p/J \tag{41}$$

where k_p is a constant coefficient, which is scaled by the inverse of J to adjust the gains for varying configuration.
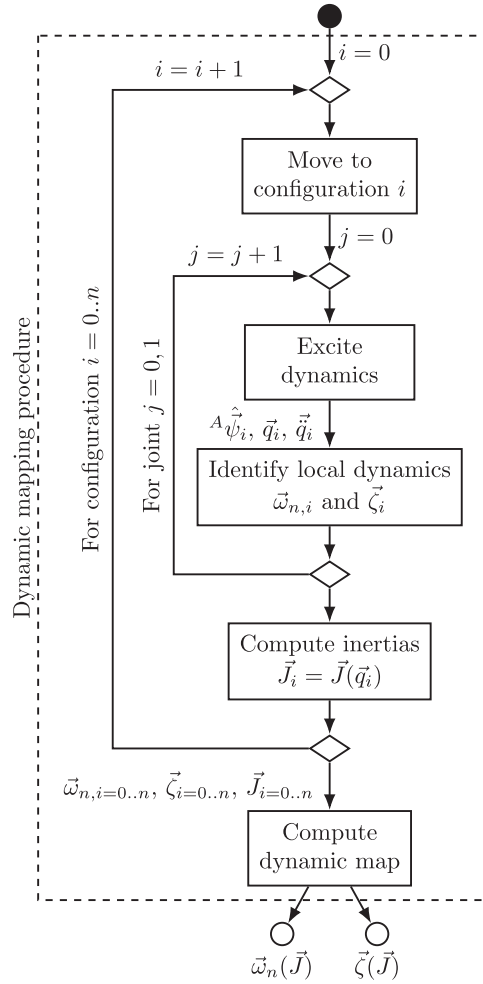
Fig. 16. Dynamic mapping procedure.

4.5.4. Dynamic map formulation

The closed loop dynamics can be described by inserting (30), (40), and (41) into (20) and (21) as:

$$\omega_n \approx \sqrt{1 + k_p/J} \; \sqrt{(k_0 + k_J J + k_g |\tau_g|)/J} \tag{42}$$

$$\zeta \approx \sqrt{1 + k_p/J} \; \frac{\left(c_0 + c_1\sqrt{J} + c_2 J\right)(1 + c_\tau J)}{2\sqrt{(k_0 + k_J J + k_g|\tau_g|)J}} \tag{43}$$

where $J = J_0$ in the base map and $J = J_1$ in the shoulder map. Thus it is desired to fit the parameters k_0, k_J, k_g, k_p, c_0, c_1, c_2, and c_τ for the base and shoulder joint respectively, to obtain a dynamic map of the vibration modes in these two directions. The overall mapping procedure is summarized by Fig. 16.

Thus a new dynamic mapping procedure has been developed and presented. The next section presents the practical setup experimental results.

5. Experiment - dynamic map

To validate the new method for dynamic mapping, an experiment is conducted. The aim of this experiment is to obtain a dynamic map of a UR5e robot, and quantify the applicability of the obtained map.

5.1. Mapping setup

An experimental setup is used for generating empirical data for the dynamic map. The setup is presented in Fig. 17. Here it is seen, how a UR5e robot is mounted on a steel stand. The steel stand is considered very rigid in comparison with the
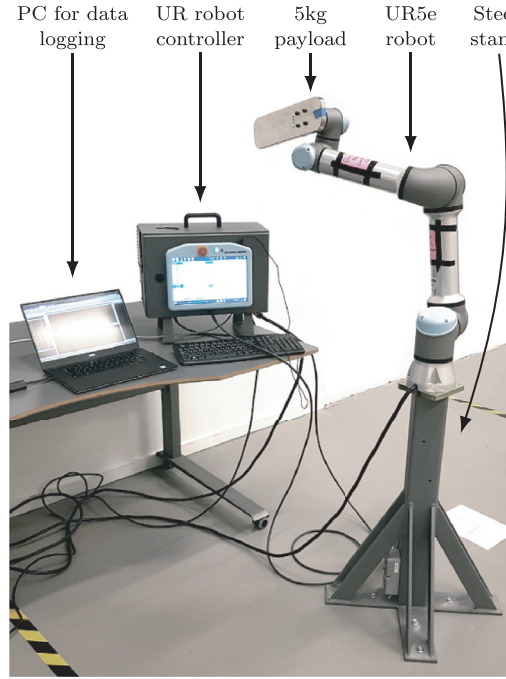
Fig. 17. Test setup with UR5e robot on stand [19].

robot itself. A payload is mounted on the tool flange. The pictured setup is with a 5kg payload, which is the rated maximum payload for the UR5e robot.

The payload is varied between 0, 1, 3, and 5kg in the experiments. The UR5e robot arm is controlled by a UR robot controller, which is shipped with the robot, and a laptop PC is used for data logging.

5.2. Generating empirical data

This subsection elaborates on the practical approach to generate the necessary data for the dynamic map. Two different algorithms are utilized for data generation. Algorithm 1 is for placing the robot in different configurations covering the

---

Algorithm 1 Dynamic mapping program for UR5e.

---

for $V = \begin{bmatrix} 0 & \pi/4 & \cdots & 3\pi/4 \end{bmatrix}$ **do**
    move TCP position to angle V
    for $R = \begin{bmatrix} 0.4 & 0.4 + 1/24 & \cdots & 0.9 \end{bmatrix}$ **do**
        move TCP position to radius R
        $j = \text{random} \begin{bmatrix} 3 & 4 & 5 \end{bmatrix}$
        Orient joint j randomly
        Identify local dynamics (Algorithm~2)
    end for
end for

---

workspace of the robot, and Algorithm 2 generates random target motions to excite vibrations in the robot, and identify f_n and ζ around the base and shoulder joints.

In Algorithm 1, the robot places the center of its tool flange in an angle, V, like illustrated in Fig. 18. Then for each value of V, the tool flange is placed in different distances between shoulder axis and center of tool flange. Thereby, the whole workspace of the robot is covered. The mapping with Algorithm 1 is repeated for each payload (0kg, 1kg, 3kg, 5kg), and in each configuration, the robot dynamics are excited and identified by Algorithm 2. This means, that the identification will be performed for 4 values of V, 13 values of R, and 4 values of payload, leading to $4 \times 13 \times 4 = 208$ different configurations. In each configuration, Algorithm 2 will run for ~ 8.5 s for each direction (base and shoulder). With overhead for motion between configurations of around 2 s, and overhead for manual payload change of around 90 s, the complete mapping procedure takes $\sim 208 \times (2 \times 8.5 + 2) + 4 \times 90 = 4312$ s ≈ 72 minutes.

The dynamics around the base and shoulder joints, respectively, are excited and identified by Algorithm 2. Many different approaches exist to excite the dynamics. For example, it is possible to use external equipment, such as a shaker of impact
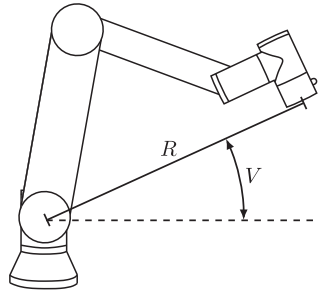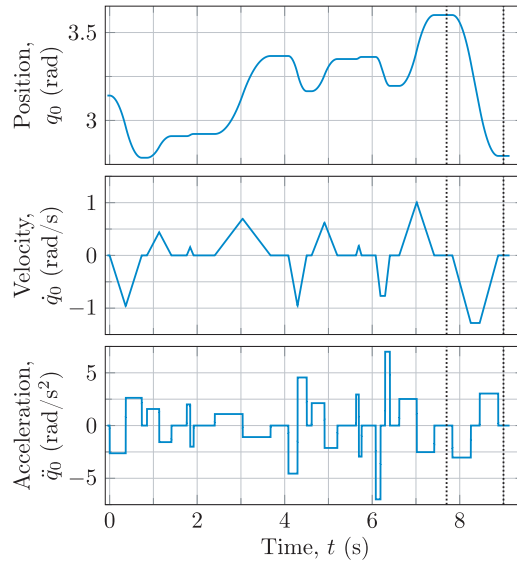

Algorithm 2 Identify local dynamics.

---

for $j = \begin{bmatrix} 0 & 1 \end{bmatrix}$ **do**
    q_{j0} = actual q_j
    Start data logging, $t = 0s$
    while $t < 8s$ **do**
        δq_j = random$(-\pi/18, \pi/18)$ rad
        $\dot{q}_j$ = random$(0.5, 2)$ rad/s
        $\ddot{q}_j$ = random$(0.3, 7)$ rad/s^2
        movej$(q_{j0} + \delta q_j, \dot{q}_j, \ddot{q}_j)$
        Wait random$(0.1, 1.0)$ s
    end while
    Stop data logging
    Fit transfer function $G_{\text{local}}(s)$ (17) to data
    Store ω_n and ζ
end for

Fig. 18. Robot pose during mapping.

Fig. 19. Random bang-coast-bang excitation reference signal for local dynamics identification.

hammer. However, it is beneficial to use the joint actuators for excitement for three primary reasons: 1) No additional hardware is needed, 2) a simple automatic process can be achieved by robot programming, 3) joint target accelerations, $\ddot{q}$, are known and can be used to identify the transfer function.

Common signals for excitation are Filtered Gaussian White Noise and Pseudo Random Binary Signal [53]. The excitation signal should be employed as a joint acceleration signal, $\ddot{q}(t)$, for identification of the robot dynamics. However, it is not readily possible to define a joint acceleration signal, using the provided interface. Instead, a sequence of random bang-coast-bang motions is used. Here a bang-coast-bang motion denotes a motion with constant joint accelerations, possibly followed by a period of constant joint velocity, finalizing with a constant deceleration [54].
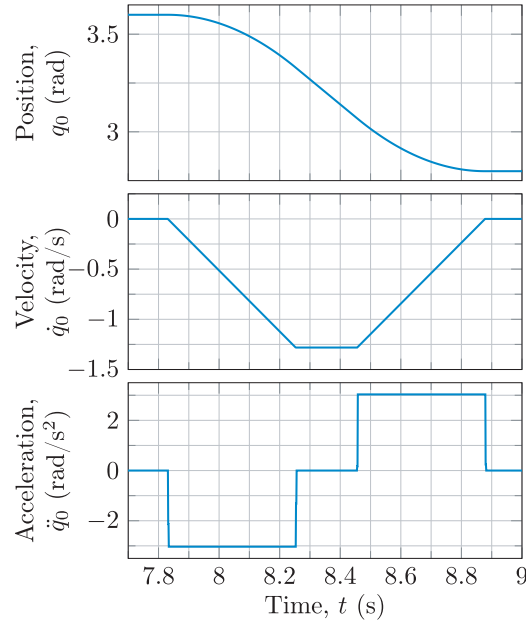
Fig. 20. Bang-coast-bang trajectory example from Fig. 19.

An example of excitation signal for the base joint is presented in Fig. 19. Here the dotted lines mark a single bang-coast-bang motion, which is presented separately in Fig. 20. The resulting joint acceleration signal in Fig. 19 is similar to a Filtered Gaussian White Noise signal, and simple to implement for a UR robot.

Target motion, i.e. q, $\dot{q}$, and $\ddot{q}$, and accelerometer measurements are logged during the motion and utilized for identification by fitting the parameters of the transfer function in (17).

5.3. Mapping results

After generating the necessary data on estimated local dynamics, i.e. for multiple independent configurations, it is possible to estimate the configuration dependency of the dynamics by fitting the coefficients of natural frequency and damping of the closed loop system in (42) and (43). This process is performed for the base and shoulder, respectively.

Early in the data processing, it was realized, that influence from c_1 and k_g were negligible. This was observed from very small numerical values and high solver uncertainty for these parameters. Thus they have been neglected in the dynamic map, and the final map formulation is:

$$\omega_n \approx \sqrt{1 + k_p/J} \, \sqrt{(k_0 + k_J J)/J} \tag{44}$$

$$\zeta \approx \sqrt{1 + k_p/J} \, \frac{(c_0 + c_2 J)(1 + c_\tau J)}{2\sqrt{(k_0 + k_J J)J}} \tag{45}$$

5.3.1. Base dynamic map

The initial results for the natural frequency around the base joint were found by fitting the parameters of:

$$\omega_{n,0} \approx \sqrt{1 + k_p/J_0} \, \sqrt{(k_0 + k_J J_0)/J_0} \tag{46}$$

where index $\{\}_0$ refers to the base joint (joint 0). The expression is found by substituting J with J_0 in (42). The results are presented in Fig. 21. Here, the correlation between natural frequency and base inertia is not convincing.

These findings motivated a changed perspective on the system dynamics around the base joint of the robot. A low inertia around the base joint, can be experienced, even though the robot is in a stretched configuration, with reference to the robot configuration in Fig. 22. An acceleration in the base joint or the shoulder joint will cause a tool acceleration in almost the same direction, i.e. ψ^0 and ψ^1 are nearly collinear, as illustrated. Also, intuitively, a configuration like seen in Fig. 22 will have a low natural frequency in any direction, including the direction around the base joint.

Thus, it was expected, that the shoulder inertia would be a better predictor of the natural frequency around the base joint. Again, please be aware that this is not a strict derivation, but a physical interpretation of the present mechanical system. Then, the coefficients of:

$$\omega_{n,0} \approx \sqrt{1 + k_p/J_1} \, \sqrt{(k_0 + k_J J_1)/J_1} \tag{47}$$
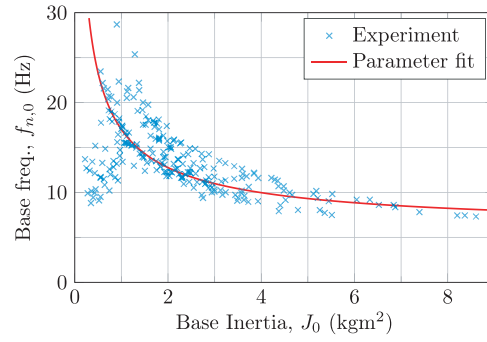
Fig. 21. Base natural frequency, $f_{n,0}$, experimental results for fitting to base inertia.
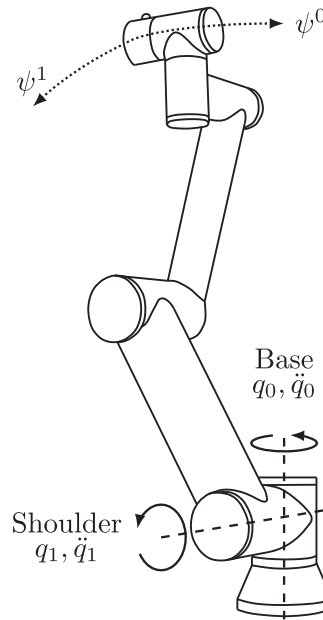

Fig. 22. Configuration with low base inertia and large shoulder inertia.

Table 1
Fitted coefficients of (47) and (48) for base dynamic map, $\omega_{n,0}$ and ζ_0. •Fixed value of k_0 to avoid overparameterization.

Parameter		Value	Unit
Stiffness	k_0	10000•	Nm/rad
Inertia coeff.	k_J	1060	Nm/rad/kgm²
Prop. gain coeff.	k_p	2.54	kgm²
Damping coeff.	c_0	1.53	Nms
Velocity coeff.	c_2	0.39	Nms/kgm²
Torque coeff.	c_τ	3.81	(kgm²)⁻¹

were identified. In the identification process, it was found that the solution space is floating, due to overparameterization. The solution space is floating because ω_n is dependent on a ratio, which can be found be infinitely many combinations. Thus, k_0 is fixed at a value of 10,000 Nm/rad to encounter the overparameterization, leaving k_J and k_p to be optimized. Then the damping ratio of vibration around the base joint is found by fitting:

$$\zeta_0 \approx (1 + k_p/J_0) \frac{(c_0 + c_2 J_0)(1 + c_\tau J_0)}{2\sqrt{(k_0 + k_J J_1)J_1}\sqrt{1 + k_p/J_1}} \tag{48}$$
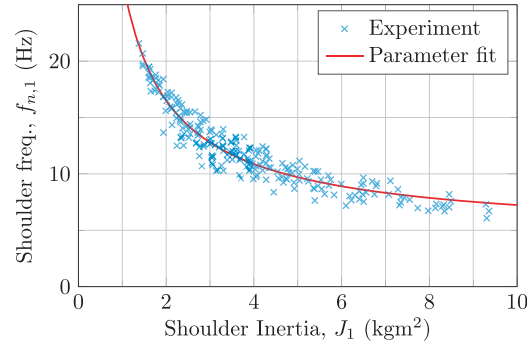
to the data, where k_0, k_J, and k_p are set to the values found in the frequency identification. The resulting coefficients of (47) and (48) are listed in Table 1, and the identified descriptions are presented in Figs. 23 and 24.
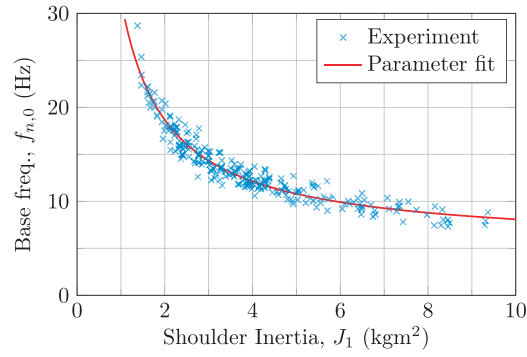
Fig. 23. Base natural frequency, $f_{n,0}$, experimental results.
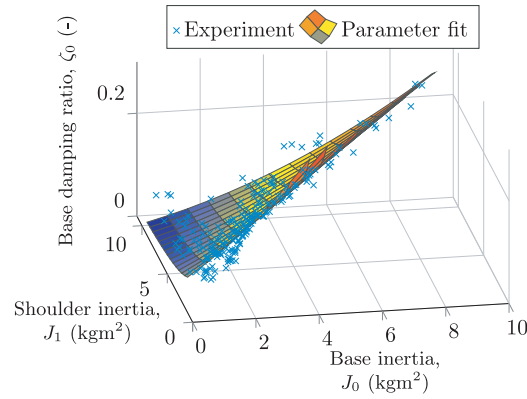
Fig. 24. Base damping ratio, ζ_0, experimental results.

Fig. 25. Shoulder natural frequency, $f_{n,1}$, experimental results.

The plotted frequency in Hz, f_n, can by found from the angular frequency, ω_n, as:

$$f_n = \frac{\omega_n}{2\pi} \tag{49}$$

5.3.2. Shoulder dynamic map

The same identification procedure of map coefficients is performed for the dynamics in shoulder direction. The natural frequency and damping ratio in shoulder direction is fitted to:

$$\omega_{n,1} \approx \sqrt{1 + k_p/J_1} \ \sqrt{(k_0 + k_J J_1)/J_1} \tag{50}$$

$$\zeta_1 \approx \sqrt{1 + k_p/J_1} \ \frac{(c_0 + c_2 J_1)(1 + c_\tau J_1)}{2\sqrt{(k_0 + k_J J_1)J_1}} \tag{51}$$

and the resulting coefficients of (50) and (51) are listed in Table 2, and the identified descriptions are presented in Figs. 25 and 26.

Table 2
Fitted coefficients of (50) and (51) for shoulder dynamic map, $\omega_{n,1}$ and ζ_1. *Fixed value of k_0 to avoid overparameterization.

Parameter		Value	Unit
Stiffness	k_0	10000*	Nm/rad
Inertia coeff.	k_J	763	Nm/rad/kgm^2
Prop. gain coeff.	k_p	1.73	kgm^2
Damping coeff.	c_0	0.27	Nms
Velocity coeff.	c_2	0.038	Nms/kgm^2
Torque coeff.	c_τ	47.2	(kgm^2)$^{-1}$
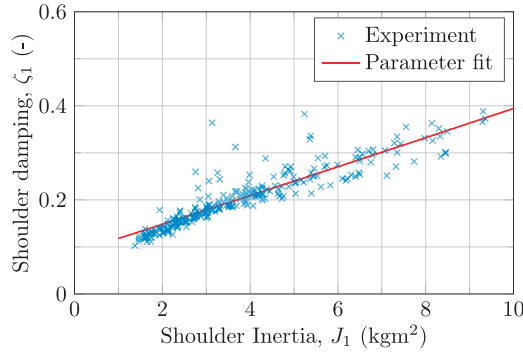
Fig. 26. Shoulder damping ratio, ζ_1, experimental results.

The next subsection evaluates the applicability, i.e. quality, of the obtained dynamic map.

5.4. Applicability evaluation

A dynamic map was obtained from experimental data in the previous subsection. However, it is not straight forward to determine whether or not the uncertainty of the estimated dynamics can be accepted. It is decided to evaluate the map quality based on robustness requirements for the multi-mode TVIST application.

It is set as a requirement, that the combination of multi-mode TVIST and the developed dynamic map, will feature a robustness to modeling error, such that the Percent Residual Vibration (PRV) will always be less than or equal to 10%. Thereby, the level of vibrations should be reduced by at least 90%. The PRV can be quantified as Singer and Seering [7], Singhose et al. [55]:

$$\text{PRV}(\omega_n, \zeta) = e^{-\zeta \omega_n \Delta_N} \sqrt{\left(C(\omega_n, \zeta)\right)^2 + \left(S(\omega_n, \zeta)\right)^2} \tag{52}$$

where ω_n is the system natural frequency, ζ is damping ratio, N is number of impulses in $I_{\text{multi-mode}}(\hat{t})$ and Δ_N is the timing of last impulse in the convolved impulse train $I_{\text{multi-mode}}(\hat{t})$. The convolved impulse train is obtained as:

$$I_{\text{multi-mode}}(\hat{t}) = (I_{\text{base}} * I_{\text{shoulder}})(\hat{t}) \tag{53}$$

and the two components are found as:

$$C(\omega_n, \zeta) = \sum_{i=1}^{N} A_i e^{\zeta \omega_n \Delta_i} \cos\left(\omega_n \sqrt{1 - \zeta^2} \Delta_i\right) \tag{54}$$

$$S(\omega_n, \zeta) = \sum_{i=1}^{N} A_i e^{\zeta \omega_n \Delta_i} \sin\left(\omega_n \sqrt{1 - \zeta^2} \Delta_i\right) \tag{55}$$

where A_i is the magnitude of impulse i in $I_{\text{multi-mode}}(\hat{t})$.

The computed PRV as given by (52) are presented in Fig. 27 for the map parameters in Tables 1 and 2. Here, the robustness range is presented for 3 different values of shoulder inertia $J_1 = 1.0, 3.2, 10.0$ kgm^2. The base inertia, J_0, has been fixed at 4.5 kgm^2 in order to obtain a 2D plot. Fixing J_0 is deemed to be acceptable for illustration purposes, because J_0 affects only the base damping, and 4.5 kgm^2 represents a mid range value.

The 3 different subplots of Fig. 27 show how the filter robustness changes with changing shoulder inertia. From Fig. 27 it is realized, that the PRV will be below 10%, if the actual system dynamics are within a specific range of frequency and
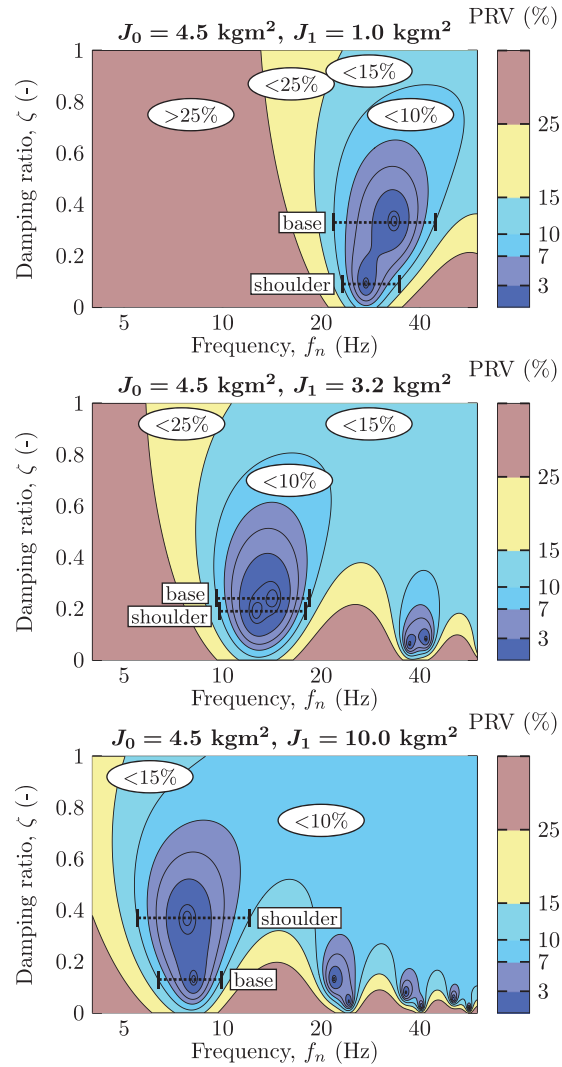
Fig. 27. Sensitivity plot for 2 mode Zero Vibration input shaping filter, presenting the Percent Residual Vibration (PRV) for 3 different values of shoulder inertia (J_1). The base inertia (J_0) is kept constant for the illustration.
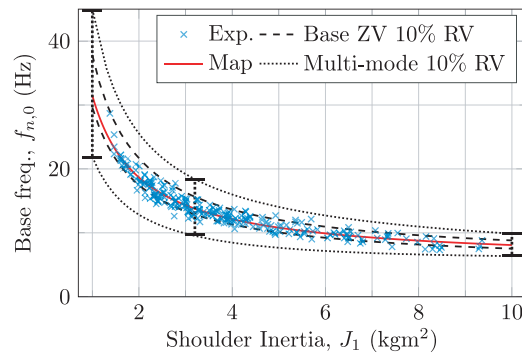
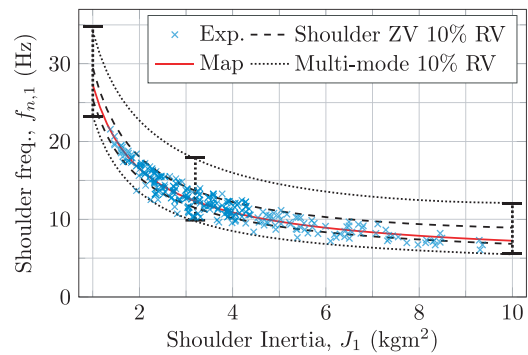**Fig. 28.** Multi-mode TVIST robustness to modeling errors in base frequency.

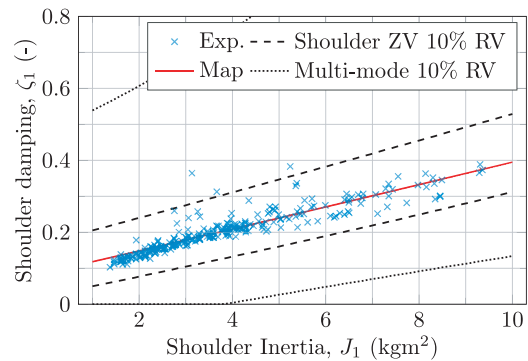**Fig. 29.** Multi-mode TVIST robustness to modeling errors in shoulder frequency.

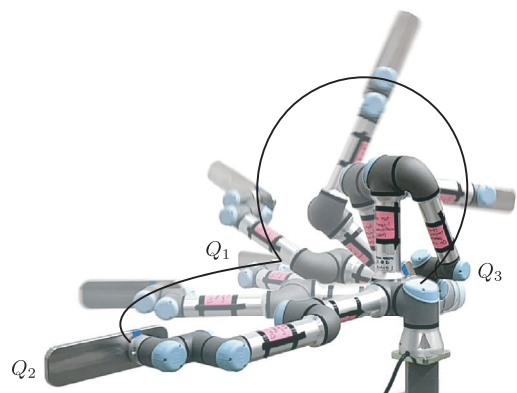**Fig. 30.** Multi-mode TVIST robustness to modeling errors in shoulder damping ratio.


Fig. 31. Q_1, Q_2, and Q_3 configurations [19].

Table 3
Listed test configurations.

	Q_1	Q_2	Q_3	
q_0	0	$\pi/2$	$\pi/2$	rad
q_1	$-\pi$	$-\pi$	$-\pi/2$	rad
q_2	0	0	$5\pi/6$	rad
q_3	$-\pi/2$	$-\pi/2$	$-\pi/2$	rad
q_4	0	0	0	rad
q_5	0	0	0	rad
J_0	9.73	9.73	1.12	kgm^2
J_1	9.25	9.25	1.58	kgm^2
$f_{d,0}$	8.01	8.01	22.0	Hz
ζ_0	0.27	0.27	0.08	–
$f_{d,1}$	6.91	6.91	19.2	Hz
ζ_1	0.37	0.37	0.14	–

Table 4
Performance of multi-mode TVIST, average of 10 repetitions.

	Delay (ms)	Res. vibration (m/s^2)
$Q_1 \rightarrow Q_2$		
Unshaped	0	0.99
Shaped	137	0.09
Impact	–	-89.5%
$Q_1 \rightarrow Q_3$		
Unshaped	0	0.77
Shaped	49	0.20
Impact	–	-73.6%
$Q_3 \rightarrow Q_1$		
Unshaped	0	1.24
Shaped	137	0.12
Impact	–	-90.3%
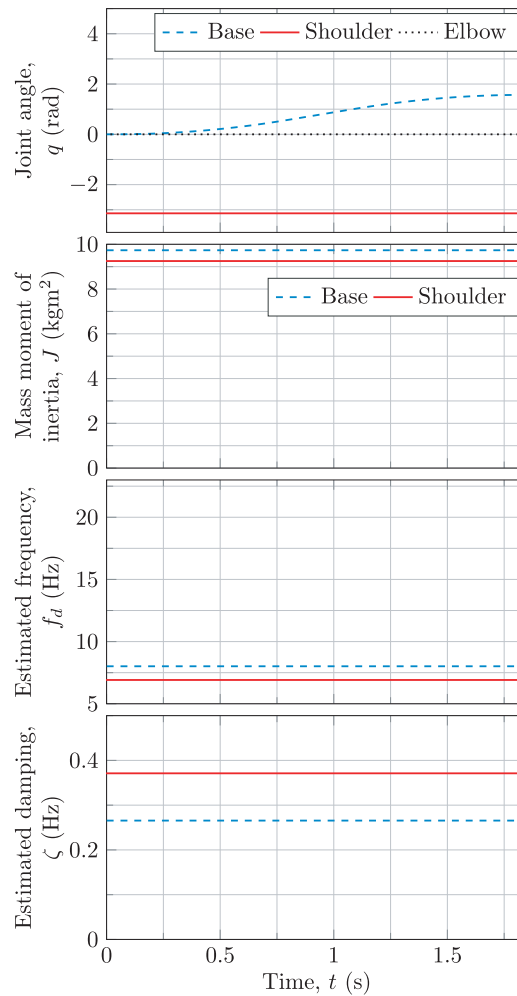
Fig. 32. Mass moment of inertia (J), estimated damped frequency (f_d), and estimated damping ratios (ζ) for test motion $Q_1 \rightarrow Q_2$.

damping from the placement of each individual filter. The robustness to modeling errors in frequency are indicated by the dotted lines for the base and shoulder, respectively. The robustness to modeling errors in damping can be found similarly.

The resulting variations in robustness to modeling errors in frequency are presented along with experimental data and dynamic map estimate in Fig. 28 for the base and in Fig. 29 for the shoulder.
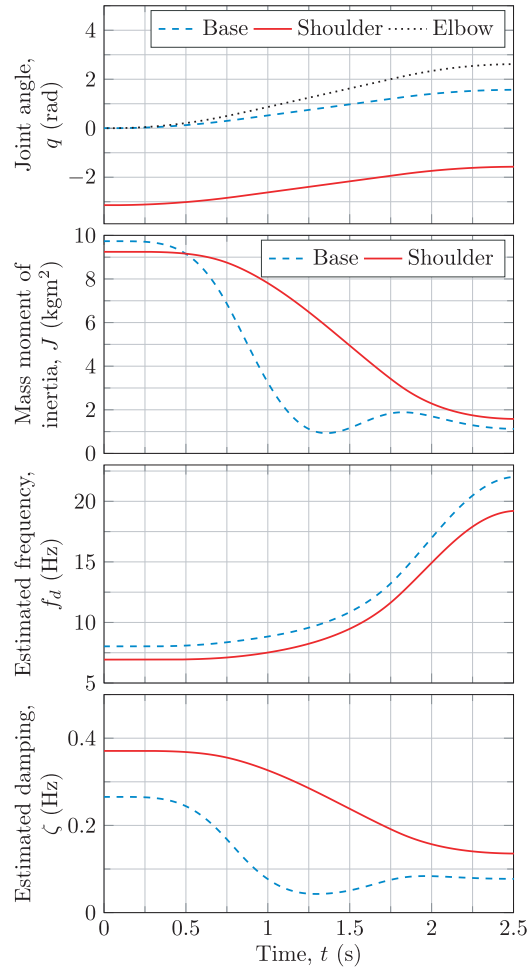
Fig. 33. Mass moment of inertia (J), estimated damped frequency (f_d), and estimated damping ratios (ζ) for test motion $Q_1 \rightarrow Q_3$.

Starting with robustness to modeling errors in base frequency in Fig. 28, two different robustness ranges are depicted in the plot: the single mode base ZV filter robustness, and the multi-mode ZV filter robustness. The sub conclusion here is, that the multi-mode TVIST filter should be able to reduce base vibrations by at least 90% for all test configurations.

It can also be seen, that the base ZV filter alone is not robust enough to meet the requirements of max 10% residual vibration.

The same sub conclusion can be made for the shoulder frequency in Fig. 29: That the multi-mode TVIST filter should be able to reduce shoulder vibrations by at least 90% for all tested configurations, but that a single mode shoulder ZV filter will not suffice.

Robustness towards modeling errors in shoulder damping ratio is presented in Fig. 30. Here, it is actually seen, that even a single mode shoulder ZV filter will be robust enough to meet the requirements of max 10% residual vibration. The multi-mode filter is extremely robust to modeling errors in damping ratio, which is also seen from Fig. 27. Thus the shoulder damping estimate is deemed to be suitable for the application.

The robustness towards modeling errors in base damping has not been considered in this evaluation. The base damping is a function of 2 variables, namely base inertia, J_0, and shoulder inertia, J_1 as seen from (48), thus other tools for analysis must potentially be chosen. The large robustness towards shoulder damping error indicates, that no further analysis is necessary for the robustness towards base damping error.

To summarize, the dynamic map for the UR5e robot has been showed to be a sufficiently accurate estimate to for multi-mode TVIST. This is concluded because the vibration level can be reduced by at least 90% for all the tested configurations in the experiment.

Thus it has been shown, that by seeing the robotic system as a whole, it is possible to simplify things a lot, and obtain a reliable estimate of the configuration depended dynamics.

It should be noticed from Figs. 28 and 29, that the system frequencies vary so much, that a time-invariant input shaping filter would need to handle a frequency range of 7–30 Hz in order to provide acceptable vibration suppression for the whole
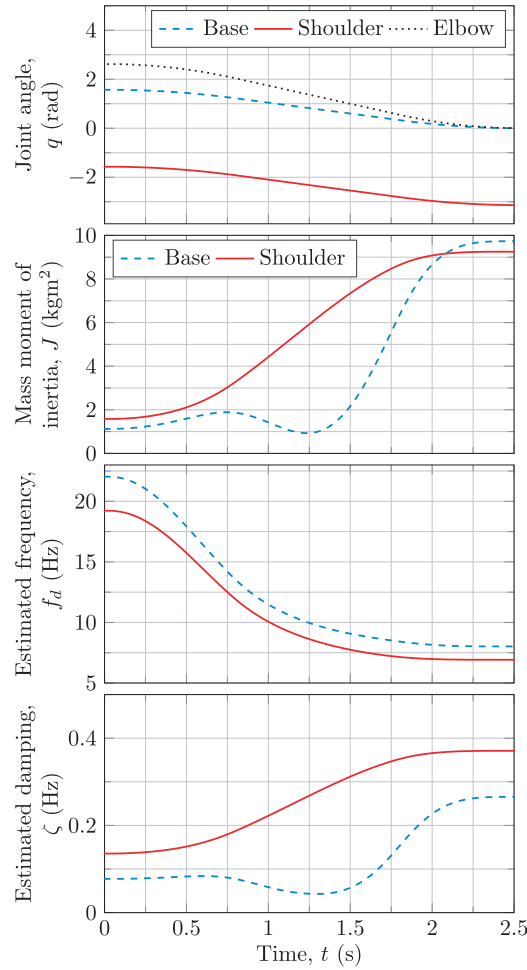
Fig. 34. Mass moment of inertia (J), estimated damped frequency (f_d), and estimated damping ratios (ζ) for test motion $Q_3 \rightarrow Q_1$.

workspace. This level of robustness can be obtained by adding more impulses, but this comes with the price of significant increase of time-delay [56]. This clearly demonstrates the practical need for TVIST methods in lightweight robot arms.

The next section presents the experimental results of multi-mode TVIST vibration reduction.

6. Experiment - multi mode TVIST

The new multi-mode dynamic map in combination with the new discrete time multi-mode TVIST implementation enables multi-mode TVIST in the UR5e robot. After implementation in the robot, a simple test is set up to validate the performance of the combined implementation.

Other researchers have demonstrated, how input shaping in joint space will cause significant Cartesian contour errors, e.g. when following a straight line tool path [57,58]. The proposed joint space multi-mode TVIST, is intended for joint space trajectories, and therefore testing is also performed with joint space motions.

6.1. Experimental setup

It is decided to follow the test procedure presented in [19]. The test motions move the robot with a 5 kg payload between configurations Q_1, Q_2, and Q_3 with joint space linear motions. The robot configurations are illustrated in Fig. 31 and listed in Table 3.

The three different joint space trajectories represent typical robot motions, which introduce large vibrations amplitudes. Two of the motions feature large variations of natural frequencies. $Q_1 \rightarrow Q_3$ going from low to high natural frequencies, and $Q_3 \rightarrow Q_1$ going from high to low. $Q_1 \rightarrow Q_2$ presents a motion with invariant natural frequencies.

In the test motions, the kinematic limitations of the double S velocity profile trajectory [54], is set as $\max(\dot{q}) = 1.5$ rad/s, $\max(\ddot{q}) = 2.0$ rad/s^2, and a jerk time, i.e. acceleration ramp up time, of 20 ms.
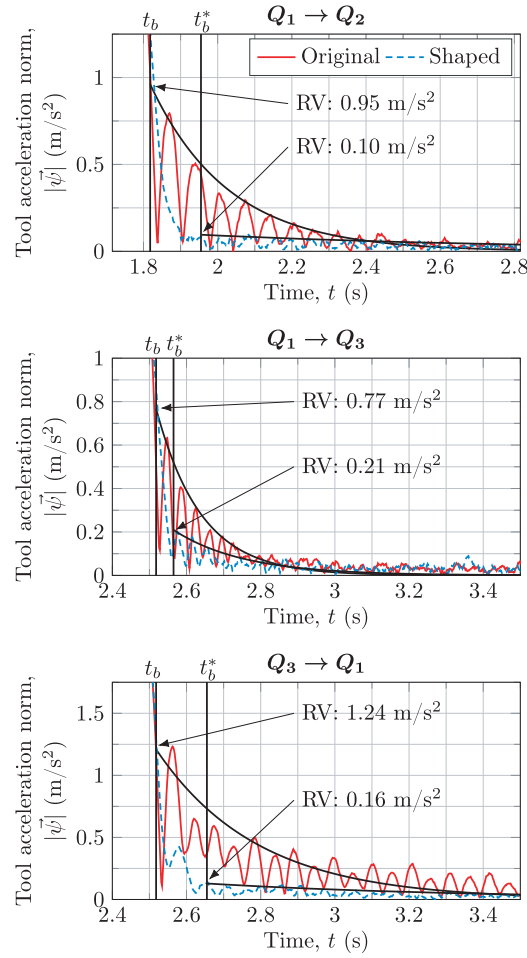
Fig. 35. Residual vibrations for test motions. Accelerations have been filtered by a moving average filter with 50 Hz cutoff frequency.

6.2. Results

The resulting mass moments of inertia seen by the joints, together with the estimated frequencies and damping ratios of the robot, based on the inertias and the dynamic map, are presented in Figs. 32–34.

The motions are shaped using the new multi-mode TVIST implementation and the estimated dynamics from the new dynamic map. The resulting impact on the residual vibrations are presented in Fig. 35, where vibrations are measured by the built-in accelerometer in the robot tool flange. The amount of Residual Vibration (RV) is quantified by extrapolating the logarithmic decay of peak accelerations back to the stop time of the motion, which is t_b for the unshaped motion and t_b^* for the shaped motion. The difference between t_b and t_b^* is the filter delay.

The experiments are repeated 10 times, and the summarized results of delay and Residual Vibration (RV) are presented in Table 4.

A more nuanced impression is gained by a frequency spectrum analysis of the residual vibrations, presented in Fig. 36.

The figure shows the vibration energy content at different frequency bands. The results are obtained by a the sum of Fast Fourier Transforms (FFT) of all acceleration components read by the accelerometer, i.e.:

$$E = \frac{\mathrm{FFT}\left({}^{A}\vec{\psi}_x\right)^2 + \mathrm{FFT}\left({}^{A}\vec{\psi}_y\right)^2 + \mathrm{FFT}\left({}^{A}\vec{\psi}_z\right)^2}{n_{\mathrm{samples}}} \tag{56}$$

where ${}^{A}\vec{\psi}_x$ is the x component of the gravity compensated accelerometer reading, $\vec{\psi}$ in its local frame, A, and n_{samples} is the number of samples in the time sequence. The presented results are average spectra from the 10 repetitions of the experiments.

The plot in Fig. 36 shows the frequency spectrum for the unshaped and shaped motion, respectively. The dashed lines indicate the estimated frequencies from Table 3.
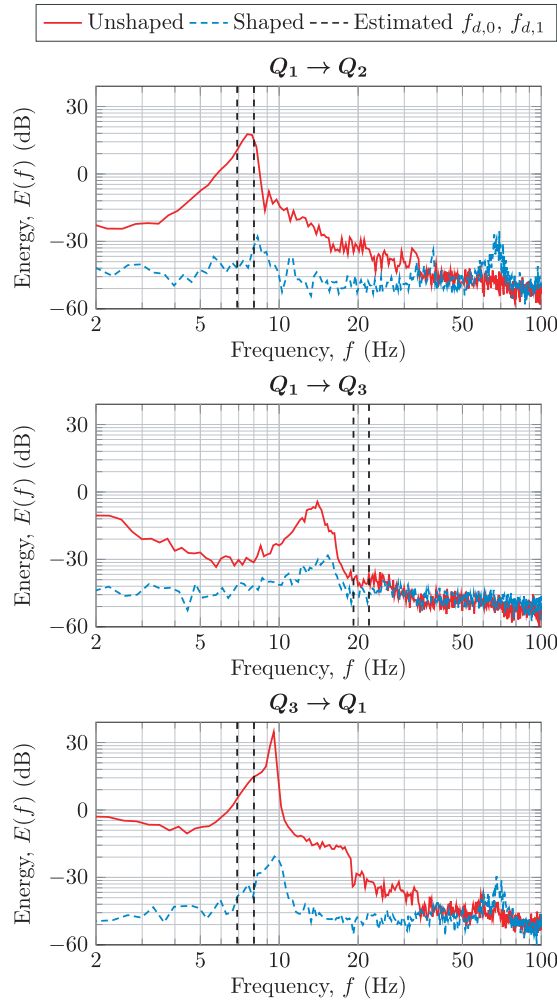
Fig. 36. Frequency spectrum analysis for test motion residual vibration. Presented spectra are averaged from Fast Fourier Transform of 10 repetitions.

6.3. Discussion on multi-mode shaping results

From both Fig. 35 and the listed results in Table 4, it is clear to see, that the proposed methods in combination can reduce the amount of residual vibration in the UR5e robot.

Starting with a visual impression of the accelerometer readings in Fig. 35, it is seen that the shaped motion has a noticeable delay. However, it is also immediately noticed, that vibrations can be reduced so much, that the resulting level of vibration will be lower.

In fact, it seems that the vibrations are reduced to the present level of noise in the application. Thus it can be concluded, that low frequency mechanical vibrations can be practically suppressed by multi-mode TVIST.

The shaped tool acceleration in Fig. 35 exhibits small acceleration amplitudes in the last part of motion. This is the Posicast control principle [10]. The shaped position target has been convolved by a vibration free set of impulses. This corresponds (nearly) to a step wise acceleration reduction near the end of motion. The *nearly* is introduced by the time-variance of the impulse sequence.

The amount of residual vibration listed in Table 4 confirms, that this is the case for the 10 repetitions of the tested motions. The $Q_1 \rightarrow Q_3$ motion, i.e. motion towards higher frequencies, shows a vibration reduction around 75%. It is seen, that motions $Q_1 \rightarrow Q_2$ and $Q_3 \rightarrow Q_1$, i.e. low frequency end configuration, have a reduced level of vibration by ~ 90%.

The employed TVIST method introduce a time-delay in the reference motion, as listed in Table 4. Generally, time-delay is not desired in industrial robots, because it decreases productivity. However, it depends on the actual task of the robot. As seen from Fig. 35, there is a significant time-delay for all motions, but the robot end-effector comes to a physical standstill at an earlier point in time. Thus, the time-delay pays of, and effectively increases the robot productivity.

The spectral analysis presented in Fig. 36 shows a few important points:

First, the approximations of two dominant vibration modes appear to hold for the test motions, seen from two energy peaks around the estimated frequencies for motions $Q_1 \rightarrow Q_2$ and $Q_3 \rightarrow Q_1$.

Second, the estimated frequencies are close to the energy peaks for motions $Q_1 \rightarrow Q_2$ and $Q_3 \rightarrow Q_1$, indicating a valid estimate in configuration Q_1 and Q_2. However, the frequency estimates for motion $Q_1 \rightarrow Q_3$ are significantly higher than the energy peaks. Thus it seems, that frequencies are overestimated for configuration Q_3. This frequency overestimate is probably the reason for the less good vibration suppression capabilities in motion $Q_1 \rightarrow Q_3$ of 74% reduction, listed in Table 4.

Third, it is seen, that the dominant energy peaks are reduced by about one order of magnitude for all motions, supporting the results of 90% vibration reduction seen in Fig. 35.

Fourth, the shaped spectra for motions $Q_1 \rightarrow Q_2$ and $Q_3 \rightarrow Q_1$ have additional energy peaks at higher frequencies. This was unexpected, but is assumed, that the high frequency oscillations appear because the low frequency oscillations are not dominating, or because the time-varying filter introduce numerical noise.

7. Conclusions

We present a practical and efficient strategy for reducing residual vibrations in robot arms by a novel Multi-Mode Fractional Delay Time-Varying Input Shaping Technology (Multi-Mode FD-TVIST), which is enabled by a novel dynamic map for the estimation of configuration-dependent vibrational characteristics with the consideration of joint and link flexibility. The new methods are validated by experimental implementation in an industrial robot from Universal Robots A/S.

First, the novel Multi-Mode FD-TVIST is proposed by combining known methods from Multi-Mode Input Shaping and FD-TVIST. The new method can reduce the residual vibration of lightweight industrial robot manipulators, if an estimator is available for the configuration-dependent multi-mode vibrations.

Second, a novel dynamic map is developed to estimate the configuration-dependent vibrational parameters (natural frequencies and damping ratios) of the two dominant vibration modes of lightweight robot manipulators. The map formulation is derived through strategic simplification of the non-linear complicated dynamics into dominant vibration modal dynamics. The principle and the procedure of the dynamic mapping have been presented with technical and theoretical details.

Third, a novel identification method for quantification of local dynamics is developed for robot arms with an accelerometer, preferably near the tool flange. The new method utilize target accelerations and actual tool accelerations to estimate a transfer function, from which the natural frequency and damping ratio can be extracted.

Fourth, a novel identification method for determining the coefficients of the dynamic map is developed, utilizing the new local dynamics identification methods in multiple configurations in the workspace of the robot.

This method completes the new toolbox of three new methods for: dynamic map description, local dynamics identification, and dynamic map identification. The strong combination provides a practical, physically sound, and time-effective approach to the establishment of a multi-mode dynamics estimator, which is accurate and computationally efficient with only few coefficients.

Fifthly, the new suite of methods for vibrational characteristics estimation is experimentally validated on a UR5e robot to be sufficiently accurate for Multi-Mode FD-TVIST.

The new Multi-Mode FD-TVIST in combination with the new multi-mode dynamic map delivers an efficient vibration suppression strategy, which is robust, simple to implement, non-sensitive to trajectory generation method, computationally cheap, and with short time-delay.

Finally, the new Multi-Mode FD-TVIST has been experimentally implemented and tested in combination with the developed dynamics estimator. The experimental results validate the new methods individually and combined. The experimental results shows that the residual vibration of the UR5e robot manipulator has been successfully reduced by up to 90% when the robot manipulator performs high-speed point-to-point operations. Our ongoing research work includes:

- extension of Multi-Mode FD-TVIST to handle Cartesian motions,
- performance comparison of Multi-Mode TVIST against smooth trajectories, such as jerk or snap limited motions,
- increased resolution dynamic mapping to investigate the importance of this factor,
- dynamic mapping of other lightweight robots,
- investigation of potential benefits of suppressing additional vibration modes in by Multi-Mode TVIST,
- quantification of the Multi-Mode TVIST impact on total robot energy consumption, and
- analysis of the Multi-Mode TVIST impact on mechanical wear of the robot components.

Declaration of Competing Interest

The authors declare that they have no known competing financial interests or personal relationships that could have appeared to influence the work reported in this paper.

Acknowledgment

References

[1] ISO 8373:2012(en) Robots and robotic devices – Vocabulary, 2012.

[2] Interact Analysis, The Industrial Robot Market - 2018, Technical Report, 2018.

[3] W. Book, Controlled motion in an elastic world, J. Dyn. Syst. Measur. Control Trans. ASME 115 (2B) (1993) 252–261, doi:10.1115/1.2899065.

[4] W. Singhose, W. Seering, N. Singer, Residual vibration reduction using vector diagrams to generate shaped inputs, 1994 J. Mech. Des. 116 (2) (1994), doi:10.1115/1.2919428.

[5] C. Conker, A. Kilic, S. Mistikoglu, S. Kapucu, H. Yavuz, An enhanced control technique for the elimination of residual vibrations in flexible-joint manipulators, Strojniški vestnik-J. Mech. Eng. 60 (9) (2014) 592–599, doi:10.5545/sv-jme.2014.1698.

[6] P. Besset, R. Béarée, FIR Filter-based online jerk-constrained trajectory generation, Control Eng. Pract. 66 (2017) 169–180, doi:10.1016/j.conengprac.2017.06.015.

[7] N.C. Singer, W.P. Seering, Preshaping command inputs to reduce system vibration, J. Dyn. Syst. Meas. Control 112 (1) (1990) 76–82, doi:10.1115/1.2894142.

[8] W.E. Singhose, W.P. Seering, N.C. Singer, Shaping inputs to reduce vibration: a vector diagram approach, in: Proceedings., IEEE International Conference on Robotics and Automation, 1990, pp. 922–927 vol.2, doi:10.1109/ROBOT.1990.126108.

[9] W. Singhose, J. Vaughan, Reducing vibration by digital filtering and input shaping, IEEE Trans. Control Syst. Technol. 19 (6) (2011) 1410–1420, doi:10.1109/TCST.2010.2093135.

[10] O.J.M. Smith, Posicast control of damped oscillatory systems, Proc. IRE 45 (9) (1957) 1249–1255, doi:10.1109/JRPROC.1957.278530.

[11] H. Ghorbani, B. Tarvirdizadeh, K. Alipour, A. Hadi, Near-time-optimal motion control for flexible-link systems using absolute nodal coordinates formulation, Mech. Mach. Theory 140 (2019) 686–710, doi:10.1016/j.mechmachtheory.2019.06.032.

[12] P.H. Chang, H.-S. Park, Time-varying input shaping technique applied to vibration reduction of an industrial robot, Control Eng. Pract. 13 (1) (2005) 121–130, doi:10.1016/j.conengprac.2004.02.009.

[13] W. Chatlatanagulchai, V.M. Beazel, P.H. Meckl, Command shaping applied to a flexible robot with configuration-dependent resonance, in: 2006 American Control Conference, 2006, doi:10.1109/ACC.2006.1656475.

[14] A. Kivila, Modeling, estimation and control for serial flexible robot arms, Georgia Institute of Technology, 2017 Ph.D. thesis.

[15] D.P. Magee, W.J. Book, The application of input shaping to a system with varying parameters, in: Japan/USA Symposium on Flexible Automation, 1, 1992, pp. 519–526.

[16] B.W. Rappole, Minimizing residual vibrations in flexible systems, MIT Artificial Intelligence Laboratory, 1992 Master's thesis.

[17] B.R. Murphy, I. Watanabe, Digital shaping filters for reducing machine vibration, IEEE Trans. Robot. Autom. 8 (2) (1992) 285–289, doi:10.1109/70.134281.

[18] D.K. Thomsen, R. Søe-Knudsen, D. Brandt, O. Balling, X. Zhang, Smooth online time-varying input shaping with fractional delay FIR filtering, Control Eng. Pract. 88 (2019) 21–37, doi:10.1016/j.conengprac.2019.04.003.

[19] D.K. Thomsen, R. Søe-Knudsen, D. Brandt, X. Zhang, Experimental implementation of time-varying input shaping on UR robots, in: Proceedings of the 16th International Conference on Informatics in Control, Automation and Robotics (ICINCO 2019), 1, 2019, pp. 488–498, doi:10.5220/0007834504880498.

[20] J. Kim, E.A. Croft, Preshaping input trajectories of industrial robots for vibration suppression, Robot. Comput. Integr. Manuf. 54 (2018) 35–44, doi:10.1016/j.rcim.2018.05.009.

[21] M. Benosman, G. Le Vey, Control of flexible manipulators: a survey, Robotica 22 (2004) 533–545, doi:10.1017/S0263574703005642.

[22] H. Rahimi, M. Nazemizadeh, Dynamic analysis and intelligent control techniques for flexible manipulators: a review, Adv. Rob. 28 (2) (2014) 63–76, doi:10.1080/01691864.2013.839079.

[23] S.K. Dwivedy, P. Eberhard, Dynamic analysis of flexible manipulators, a literature review, Mech. Mach. Theory 41 (7) (2006) 749–777, doi:10.1016/j.mechmachtheory.2006.01.014.

[24] M. Liang, B. Wang, T. Yan, Dynamic optimization of robot arm based on flexible multi-body model, J. Mech. Sci. Technol. 31 (8) (2017) 3747–3754, doi:10.1007/s12206-017-0717-9.

[25] T. Hardeman, R. Aarts, B. Jonker, Modelling and identification of robots with joint and drive flexibilities, Solid Mech. Applica. 130 (2005) 173–182, doi:10.1007/1-4020-4161-6_15.

[26] S. Moberg, E. Wernholt, S. Hanssen, T. Brogårdh, Modeling and Parameter Estimation of Robot Manipulators Using Extended Flexible Joint Models, Journal of Dynamic Systems, Measurement, and Control 136 (3) (2014), doi:10.1115/1.4026300. 031005

[27] R.D. Neidinger, Multivariate polynomial interpolation in newton forms, SIAM Rev. 61 (2) (2019) 361–381, doi:10.1137/17M1124188.

[28] A. Hoevenaars, S. Krut, J. Herder, Jacobian-based natural frequency analysis of parallel manipulators, Mech. Mach. Theory 148 (2020) 103775, doi:10.1016/j.mechmachtheory.2019.103775.

[29] W. Singhose, Command shaping for flexible systems: a review of the first 50 years, Int. J. Precis. Eng. Manuf. 10 (4) (2009) 153–168, doi:10.1007/s12541-009-0084-2.

[30] C. Conker, H. Yavuz, H.H. Bilgic, A review of command shaping techniques for elimination of residual vibrations in flexible-joint manipulators, J. Vibroeng. (2016), doi:10.21595/jve.2016.16725.

[31] S.W. Smith, The Scientist & Engineer's Guide to Digital Signal Processing, California Technical Pub, 1997.

[32] J.M. Hyde, W.P. Seering, Using input command pre-shaping to suppress multiple mode vibration, in: Proceedings. 1991 IEEE International Conference on Robotics and Automation, 1991, pp. 2604–2609 vol.3, doi:10.1109/ROBOT.1991.132020.

[33] D.P. Magee, W.J. Book, Eliminating multiple modes of vibration in a flexible manipulator, in: [1993] Proceedings IEEE International Conference on Robotics and Automation, 1993, pp. 474–479 vol.2, doi:10.1109/ROBOT.1993.291912.

[34] H. Yavuz, S. Mistikoglu, S. Kapucu, Hybrid input shaping to suppress residual vibration of flexible systems, J. Vib. Control 18 (1) (2012) 132–140, doi:10.1177/1077546311403179.

[35] J.-K. Cho, Y.-S. Park, Vibration reduction in flexible systems using a time-varying impulse sequence, Robotica 13 (3) (1995) 305–313, doi:10.1017/S0263574700017835.

[36] R.C. Dorf, R.H. Bishop, Modern control systems, 12th, Prentice Hall, 2010.

[37] A. Jubien, M. Gautier, A. Janot, Dynamic identification of the Kuka LWR robot using motor torques and joint torque sensors data, IFAC Proceedings 47 (3) (2014) 8391–8396, doi:10.3182/20140824-6-ZA-1003.01079. 19th IFAC World Congress

[38] S. Mejri, V. Gagnol, T.-P. Le, L. Sabourin, P. Ray, P. Paultre, Dynamic characterization of machining robot and stability analysis, Int. J. Adv. Manuf. Technol. 82 (1–4) (2016) 351–359, doi:10.1007/s00170-015-7336-3.

[39] E. Wernholt, S. Gunnarsson, Analysis of methods for multivariable frequency response function estimation in closed loop, in: 2007 46th IEEE Conference on Decision and Control, 2007, pp. 4881–4888, doi:10.1109/CDC.2007.4434780.

[40] R.J. Schilling, Fundamentals of Robotics - analysis and control, Prentice Hall, 1990.

[41] T. Kurfess, Robotics and Automation Handbook, CRC Press, 2004.

[42] J.J. Craig, Introduction to Robotics - Mechanics and Control, 3rd Ed., Pearson Prentice Hall, 2005.

[43] B. Siciliano, O. Khatib, Springer Handbook of Robotics, Springer Science & Business Media, 2008, doi:10.1007/978-3-540-30301-5.

[44] J.L. Meriam, L.G. Kraige, Engineering mechanics: Dynamics, Wiley, 2006.

[45] T.D. Tuttle, Understanding and modeling the behavior of a harmonic drive gear transmission, Technical Report, Massachusetts Inst of Tech Cambridge Artificial Intelligence Lab, 1992.

[46] H. Zhang, S. Ahmad, G. Liu, Modeling of torsional compliance and hysteresis behaviors in harmonic drives, IEEE/ASME Trans. Mechatron. 20 (1) (2015) 178–185, doi:10.1109/TMECH.2014.2311382.

[47] E. Madsen, O.S. Rosenlund, D. Brandt, X. Zhang, Model-based on-line estimation of time-varying nonlinear joint stiffness on an e-series universal robots manipulator, in: 2019 International Conference on Robotics and Automation (ICRA), 2019, pp. 8408–8414, doi:10.1109/ICRA.2019.8793935.

[48] P. Raveendranath, G. Singh, B. Pradhan, A two-noded locking-free shear flexible curved beam element, Int. J. Numer. Method. Eng. 44 (2) (1999) 265–280, doi:10.1002/(SICI)1097-0207(19990120)44:2<265::AID-NME505>3.0.CO;2-K.

[49] A. Shaw, T. Hill, S. Neild, M. Friswell, Periodic responses of a structure with 3:1 internal resonance, Mech. Syst. Signal Process. 81 (2016) 19–34, doi:10.1016/j.ymssp.2016.03.008.

[50] S. Wolf, M. Iskandar, Extending a dynamic friction model with nonlinear viscous and thermal dependency for a motor and harmonic drive gear, in: 2018 IEEE International Conference on Robotics and Automation (ICRA), 2018, pp. 783–790, doi:10.1109/ICRA.2018.8460613.

[51] A.C. Bittencourt, S. Gunnarsson, Static Friction in a Robot Joint - Modeling and Identification of Load and Temperature Effects, Journal of Dynamic Systems, Measurement, and Control 134 (5) (2012), doi:10.1115/1.4006589. 051013

[52] P. Hamon, M. Gautier, P. Garrec, Dynamic identification of robots with a dry friction model depending on load and velocity, in: 2010 IEEE/RSJ International Conference on Intelligent Robots and Systems, 2010, pp. 6187–6193, doi:10.1109/IROS.2010.5649189.

[53] L. Ljung, System Identification - Theory for the User, 2nd, Prentice Hall PTR, 1999.

[54] L. Biagiotti, C. Melchiorri, Trajectory Planning for Automatic Machines and Robots, Springer-Verlag Berlin Heidelberg, 2008, doi:10.1007/978-3-540-85629-0.

[55] W. Singhose, E. Biediger, Y.-H. Chen, B. Mills, Reference command shaping using specified-negative-amplitude input shapers for vibration reduction, J. Dyn. Syst. Measur. Control Trans. ASME 126 (1) (2004) 210–214, doi:10.1115/1.1650385.

[56] J. Vaughan, A. Yano, W. Singhose, Comparison of robust input shapers, J. Sound Vib. 315 (4–5) (2008) 797–815, doi:10.1016/j.jsv.2008.02.032.

[57] Y. Liu, Y. Cao, L. Sun, X. Zheng, Vibration suppression for wafer transfer robot during trajectory tracking, in: 2010 IEEE International Conference on Mechatronics and Automation, 2010, pp. 741–746, doi:10.1109/ICMA.2010.5589042.

[58] Y. Zhao, W. Chen, T. Tang, M. Tomizuka, Zero time delay input shaping for smooth settling of industrial robots, in: 2016 IEEE International Conference on Automation Science and Engineering (CASE), 2016, pp. 620–625, doi:10.1109/COASE.2016.7743459.